

1 Simulated supercells in nontornadic and tornadic VORTEX2 environments

2 Brice E. Coffer* and Matthew D. Parker

3 Department of Marine, Earth, and Atmospheric Sciences, North Carolina State University,

4 Raleigh, NC

5 *Corresponding author address: Brice Coffer, North Carolina State University, Campus Box 8208,

6 Raleigh, NC, 27615-8208

7 E-mail: becoffer@ncsu.edu

ABSTRACT

8 The composite near-storm environments of nontornadic and tornadic supercells sampled
9 during the second Verification of the Origins of Rotation in Tornadoes Experiment (VOR-
10 TEX2) both appear to be generally favorable for supercells and tornadoes. It has not been
11 clear whether small differences between the two environments (e.g. more streamwise hori-
12 zontal vorticity in the lowest few hundred meters above the ground in the tornadic compos-
13 ite) are actually determinative of storms' tornadic potential. From the VORTEX2 compos-
14 ite environments, simulations of a nontornadic and a tornadic supercell are used to investi-
15 gate storm-scale differences that ultimately favor tornadogenesis or tornadogenesis failure.
16 Both environments produce strong supercells with robust mid-level mesocyclones and hook
17 echoes, though the tornadic supercell has a more intense low-level updraft and develops a
18 tornado-like vortex exceeding the EF3 wind speed threshold. In contrast, the nontornadic
19 supercell only produces shallow vortices, which never reach the EF0 wind speed threshold.
20 Even though the nontornadic supercell readily produces subtornadic surface vortices, these
21 vortices fail to be stretched by the low-level updraft. This is due to a disorganized low-level
22 mesocyclone caused by predominately crosswise vorticity in the lowest few hundred meters
23 ALG within the nontornadic environment. In contrast, the tornadic supercell ingests predom-
24 inately streamwise horizontal vorticity, which promotes a strong low-level mesocyclone with
25 enhanced dynamic lifting and stretching of surface vertical vorticity. These results support
26 the idea that larger streamwise vorticity establishes the base of the mesocyclone at lower al-
27 titudes, whereas predominately crosswise vorticity leads to a less favorable configuration of
28 the low-level mesocyclone for tornadogenesis.

29 **1. Introduction**

30 Since the Verification of the Origins of Rotation in Tornadoes Experiment (VORTEX; Ras-
31 mussen et al. 1994) in the mid-1990s, considerable progress has been made regarding our recogni-
32 tion of the lower tropospheric profiles of temperature, humidity, and winds that favor nontornadic
33 versus tornadic supercells (Rasmussen and Blanchard 1998; Rasmussen 2003; Markowski et al.
34 2003; Thompson et al. 2003, 2007; Craven et al. 2004). However, it is still unclear how these en-
35 vironmental differences, especially the low-level¹ wind profile, affect the in-storm processes that
36 lead to tornadogenesis.

37 Tornadogenesis within supercell thunderstorms has traditionally been thought of as a three-
38 step process: 1) development of a mid-level mesocyclone via tilting of environmental horizontal
39 vorticity into the vertical by the updraft, 2) generation of subtornadic², surface vertical vorticity
40 by a downdraft, and 3) the contraction of that surface vertical vorticity into a tornado (Davies-
41 Jones and Brooks 1993; Davies-Jones 2015). Recent research using high-resolution simulations
42 (e.g. Dahl et al. 2014; Markowski and Richardson 2014; Schenkman et al. 2014; Markowski 2016)
43 has expanded on earlier seminal work (Davies-Jones 1982; Davies-Jones and Brooks 1993) detail-
44 ing the specific processes that enable step 2) of the tornadogenesis process. However, it seems
45 that supercells produce near-ground rotation rather easily, regardless of the initial orientation of
46 the low-level winds (Dahl 2015; Parker and Dahl 2015). Observations of supercells have shown
47 remarkable resemblance between nontornadic and tornadic supercells, including similar precipi-
48 tation echoes, kinematic structures of the rear-flank outflow, and the presence of low-level meso-
49 cyclones and surface circulations (Trapp 1999; Wakimoto and Cai 2000; Wakimoto et al. 2004;

¹In this paper, “low-level” refers to the lowest ~ 1 km above ground level (AGL), while “near-surface” or “surface” will refer to 10 m (the lowest model level grid).

²Hereafter, “subtornadic vorticity” will refer to mesocyclonic scale vertical vorticity ($\geq 0.01 \text{ s}^{-1}$) at the surface.

50 Markowski et al. 2008, 2011). Despite these similarities, the majority of supercells (at least 75%)
51 do not produce tornadoes (Trapp et al. 2005). It is likely not a coincidence that the false alarm
52 rate for tornado warnings in the United States is also approximately 75% (Brotzge et al. 2011).
53 Unfortunately, we cannot yet explain what separates the ostensibly similar nontornadic supercells
54 from tornadic supercells. What are the different processes that lead to either tornadogenesis or
55 tornadogenesis failure, and can these processes be directly linked to the environment?

56 To address this gap in the knowledge base, during the second VORTEX field campaign
57 (VORTEX2; Wurman et al. 2012), numerous near-supercell observations were collected in order
58 to assess environmental variability and to further understand the relationship between the envi-
59 ronment and tornadoes. Parker (2014) generated composite environments (from 134 near-storm
60 soundings) of the 12 best sampled VORTEX2 supercells; this included 7 tornadic and 5 nontor-
61 nadic supercells. Both the nontornadic and tornadic near-inflow composite soundings from Parker
62 (2014) are seemingly favorable for tornadoes, with convective available potential energy (CAPE)
63 values greater than 2000 J kg^{-1} and storm-relative helicity (SRH) near $300 \text{ m}^2 \text{ s}^{-2}$ in the effective
64 inflow layer (Table 1). In fact, each profile has a significant tornado parameter that is above the cli-
65 matological median for EF3+ tornadoes (Thompson et al. 2012)³. The most noticeable difference
66 between the nontornadic and tornadic composites is in the low-level wind profile; specifically, the
67 orientation of the low-level shear vector implies that the tornadic cases have much more stream-
68 wise horizontal vorticity in the lowest 500 m AGL (Fig. 1).

69 While low-level SRH is typically reported in the 0 - 1 km layer, it has been previously noted
70 that even shallower layers may be more skillful for tornado forecasting (Rasmussen 2003). Using

³As noted in Parker (2014), common forecasting parameters such as low-level shear and lifted condensation level (LCL) were enhanced in the near-inflow environment, thus the soundings used herein are not a perfect comparison with the RUC-generated proximity soundings used by Thompson et al. (2003, 2012).

71 observed proximity soundings, Esterheld and Giuliano (2008) showed that SRH integrated over
72 the 0 - 500 m layer provided the best discrimination between nontornadic and tornadic supercells.
73 Additionally, the angle between the 0 - 500 m AGL shear vector and the 10 m storm-relative inflow
74 vector (referred to as the “critical angle”) was most commonly near 90 degrees for the significantly
75 tornadic supercells (indicating purely streamwise horizontal vorticity). Meanwhile for the nontor-
76 nadic supercells, the critical angle was much more frequently near 110 degrees (indicating par-
77 tially crosswise horizontal vorticity). In the VORTEX2 dataset, the 0 - 500 m SRH is considerably
78 higher in the tornadic composite compared to the nontornadic (159 vs. $80 \text{ m}^2 \text{ s}^{-2}$, respectively)
79 and, just as in Esterheld and Giuliano (2008), the critical angle is approximately 90 degrees for
80 the tornadic environment, whereas the nontornadic environment has a critical angle of 140 de-
81 grees. Increased streamwise vorticity and SRH in the lowest few hundred meters should promote
82 a stronger low-level mesocyclone in a supercell and thereby stronger dynamic lifting. This lifting,
83 in turn, may increase the likelihood of tornadogenesis (Markowski et al. 2012b; Markowski and
84 Richardson 2014; Coffer and Parker 2015). The orientation of the low-level winds in the nontor-
85 nadic cases may also alter the interaction between the cold pool and vertical wind shear, which in
86 some cases leads to an unfavorable, backward-tilted updraft orientation (Nowotarski 2015).

87 The purpose of this paper is to explore contrasting storm-scale characteristics of full-physics
88 supercell simulations initialized with the nontornadic and tornadic pair of VORTEX2 composite
89 environments. We use these simulations to address the following questions:

- 90 1. Do the two VORTEX2 composite soundings contain sufficiently distinct ingredients to “cor-
91 rectly” simulate nontornadic and tornadic supercells in the respective nontornadic and tor-
92 nadic environments?

93 2. If so, what is the failure point for tornadogenesis in the nontornadic supercell compared to
94 the tornadic supercell?

95 3. Finally, can this failure point be specifically traced to some trait that differs between the
96 nontornadic and tornadic environments?

97 The methods are described in Section 2, while general comparisons of the evolution between
98 the nontornadic and tornadic simulations are discussed in Section 3. Additionally in Section 3,
99 unique aspects of the individual supercells are detailed more comprehensively, and then specific
100 storm-scale differences that lead to tornadogenesis (or the lack thereof) are described in Section 4.
101 Clearer cause/effect is then gleaned from simpler “toy model” simulations, which are explored in
102 Section 5. We conclude with a synthesis of the main findings and avenues for future work.

103 **2. Methods**

104 *a. Model Configuration*

105 To examine potentially relevant differences between storms in the nontornadic and tornadic
106 VORTEX2 composite environments, supercell simulations were conducted using release 17 of
107 Cloud Model version 1 (“CM1”; see appendix of Bryan and Morrison 2012). These storms were
108 simulated for 2 h on a 200 x 200 x 18 km³, horizontally homogeneous domain initialized using
109 the near-inflow composite VORTEX2 soundings from Parker (2014) discussed previously (Fig.
110 1). For rapid data collection, near-storm soundings during VORTEX2 were usually terminated at
111 the approximate height of the tropopause. A potential temperature inversion of 20 K km⁻¹ with
112 1% relative humidity and constant winds was used as an approximation for stratospheric data.
113 Convection was initiated using the updraft nudging technique described by Naylor and Gilmore
114 (2012), and the simulations use a six-category, fully double-moment bulk microphysics scheme

from the National Severe Storms Laboratory (NSSL) that explicitly predicts the variable densities of hail and graupel (Ziegler 1985; Mansell 2010; Mansell et al. 2010). The horizontal grid spacing is 125 m within a 100 x 100 km² inner domain centered on the right-moving supercell and gradually increases to 3.875 km at the edges of the domain (Wilhelmson and Chen 1982). The lowest scalar grid level is at 10 m, and from there, the vertical grid spacing stretches from 20 m in the lowest 300 m to 280 m at 12 km, allowing for 31 levels in the lowest kilometer. The model time step was 0.6 s, with eight split time steps for the acoustic modes (Klemp and Wilhelmson 1978). A fifth-order advection scheme, utilizing high-order weighted essentially non-oscillatory finite differencing, is used with no additional artificial diffusion (Wicker and Skamarock 2002; Shu 2003). The subgrid-scale turbulence is parameterized by a 1.5 order turbulence kinetic energy closure scheme similar to Deardorff (1980), with separate horizontal and vertical turbulence coefficients. Open, radiative lateral boundary conditions were employed, while the upper-boundary has a rigid, free-slip boundary condition, with a Rayleigh damping sponge applied above 14 km. The bottom-boundary condition is semi-slip and is described in more detail below.

b. Semi-slip bottom boundary condition

Idealized simulations of supercell thunderstorms have almost exclusively been conducted using free-slip bottom boundary conditions. In these simulations, it has generally been found that the tilting of baroclinically generated horizontal vorticity by downdrafts near the surface produces intense, tornado-like vortices (e.g. Rotunno and Klemp 1985; Wicker and Wilhelmson 1995; Adelman et al. 1999; Dahl et al. 2014; Markowski and Richardson 2014). Observations of tornadic supercells also heavily suggest the influence of baroclinity (Markowski 2002; Markowski et al. 2012a,b; Straka et al. 2007; Marquis et al. 2012). However, recently, frictional generation of vorticity has been investigated in supercell simulations and at times been found to be an ap-

preciable contributor to the vorticity budget (Schenkman et al. 2014; Roberts et al. 2016), albeit baroclinity likely dominates once the storm's cold pool is established (Markowski 2016). It is also well-established that surface drag is crucial for disrupting cyclostrophic balance and inducing strong radial inflow into a developing tornado (Davies-Jones 2015). Although incorporating surface friction into idealized convective simulations presents difficulties (Markowski and Bryan 2016), we have applied a constant surface drag coefficient (C_d) of 0.0014 in an attempt to partially capture frictional effects on within-storm processes. This C_d value was calculated in CM1 from the composite VORTEX2 rear-flank outflow sounding (Parker 2014, see their Fig. 9) using the surface layer scheme developed by Jiménez et al. (2012), with a land-use type set to summertime “irrigated cropland” (defined by the U.S. Geological Survey). The computed value of C_d from the composite VORTEX2 near-inflow sounding was approximately 0.005, similar to those reported in Frame and Markowski (2010) and Nowotarski et al. (2015). However, the rear-flank outflow is the main area of interest for vorticity generation and tornadogenesis (e.g. Rotunno and Klemp 1985; Wicker and Wilhelmson 1995; Dahl et al. 2014; Markowski and Richardson 2014); thus the smaller C_d value (based on the outflow profile with higher static stability) was used. This smaller value of C_d also lessens the potential for surface drag to excessively modify the near-ground vertical wind shear (as examined by Markowski and Bryan 2016). Future work should investigate the effect of varying values of C_d (and roughness length), as well as different drag parameterizations, upon the development of near-ground rotation. Our philosophy is that the simple inclusion of modest surface drag represents a more physically consistent bottom boundary condition for tornadogenesis than does the habitually employed free-slip assumption.

In the absence of a large-scale pressure gradient force (PGF), surface drag continually slows the base-state low-level wind profile in idealized, horizontally homogeneous simulations. To minimize this, Coriolis force was applied to the perturbation winds. This is equivalent to assuming that

the initial wind profile is in geostrophic balance⁴ and introduces a force that opposes and offsets frictional effects once a new steady state is acquired (see equations 7-8 of Roberts et al. 2016). The Coriolis parameter was set to a typical mid-latitude value of $f = 10^{-4} \text{ s}^{-1}$. Since both surface drag and the Coriolis force affect the base-state slowly, each environmental profile was first simulated in a small-domain simulation with the same model configuration described in Section 2a (except for periodic lateral boundaries and no convection initialization). After roughly five hours, the wind profile in the lowest two hundred meters arrived at a quasi-steady state. Each of the horizontally homogeneous supercell simulations discussed herein are therefore initialized using a wind profile extracted at this time ($t = 4 \text{ h}$). The differences between the adjusted and initial profiles were rather small, especially compared to the wind profile evolution without Coriolis (Table 2, Fig. 1), and with this treatment, the far inflow environment remains nearly steady-state throughout the 2 h full-physics simulation. Although the supercells remain centered in the fine-mesh domain using a horizontal grid translation (making the model winds effectively "storm-relative"), the surface momentum fluxes were calculated using the full ground-relative wind speeds. Lower resolution supercell simulations showed similar trends in storm structure, updraft strength, and near-surface vertical vorticity evolution between supercells that traversed across a fixed domain versus those that were centered in a moving grid with this treatment.

3. Evolution of the nontornadic and tornadic supercells

a. Environmental Characteristics

The nontornadic and tornadic simulations are initialized with the near-inflow soundings (with wind profile adjustments explained in Section 2b) composited from the 5 nontornadic su-

⁴Real-world profiles include boundary layer modifications from surface drag and are therefore not truly geostrophic, but the adjustments in the wind profile are small using this assumption, as will be shown.

183 percells and 7 tornadic supercells best-observed during VORTEX2 (Parker 2014). The nontor-
184 nadic composite represents high-end null supercell cases, which are particularly problematic for
185 operational warnings and, thus, quite intriguing to analyze. Both composite soundings possess
186 ample CAPE, modest convective inhibition (CIN), low lifted condensation level (LCL) heights,
187 and sufficient deep-layer and low-level shear (Table 1). These combined ingredients lead to an
188 effective-layer supercell composite parameter (SCP) of 14.9 and 16.4 and a significant tornado pa-
189 rameter (STP) of 2.6 and 4.9 in the nontornadic and tornadic environments, respectively. In bulk,
190 the nontornadic and tornadic composite environments are rather similar and both would gener-
191 ally be considered favorable for supercells *and* tornadoes (nontornadic environments are typically
192 associated with STP values less than 1 in the model derived proximity soundings of Thompson
193 et al. 2003, 2007). While the individual parameters are slightly more impressive in the tornadic
194 environment, the differences are not particularly striking. Curiously, the effective inflow SRH, one
195 of the components of the STP, is actually higher in the nontornadic environment.

196 *b. General differences between the nontornadic and tornadic supercells*

197 For the first twenty minutes of each simulation, a large amount of precipitation develops in
198 response to the updraft-nudging initialization technique. Afterwards, in both cases, a dominant,
199 cyclonic, right-moving storm begins to take on supercellular reflectivity structures (Figs. 2, 3),
200 and weaker disorganized convection moves north into the outer-mesh (not shown). The supercell
201 initialized in the tornadic VORTEX2 environment begins to organize at low-levels 10-15 min
202 sooner than the supercell initialized in the nontornadic VORTEX2 profile. During their most
203 intense phase, the two supercells look remarkably similar in terms of reflectivity (cf. Figs. 2h,
204 3e). Both storms possess a strong updraft in the mid-levels (e.g. 4 - 5 km AGL), with vertical
205 velocities exceeding 40 m s^{-1} (Fig. 4). Despite these similarities, the low-level updraft in the

206 tornadic VORTEX2 supercell is much stronger; velocities greater than 50 m s^{-1} are occasionally
207 present as low as 500 m AGL. Since both environments have similar values of surface based CAPE
208 and CIN, these differences in the updraft velocity are likely due to dynamical influences. In turn,
209 the contrasting low-level updrafts may eventually alter the intensification of surface vortices (e.g.
210 through stretching). The nontornadic VORTEX2 supercell produces weak (never reaching the EF0
211 wind speed threshold), shallow (extending < 1 km AGL), transient (lasting a few minutes or less)
212 surface vortices (Fig. 5). In contrast, the tornadic VORTEX2 supercell develops intense, long-
213 lasting surface vortices⁵. The tornado-like vortex (hereafter, simply “tornado”)⁶ that develops at t
214 = 55 min reaches a peak surface vertical vorticity of 1.1 s^{-1} , a maximum 10 m wind speed over
215 70 m s^{-1} ($\sim 160 \text{ mph}$; corresponding to the criteria for a high-end EF3 tornado), and lasts for
216 approximately 25 min (Fig. 5). These differences between the two supercells are explored in
217 greater detail in Section 4.

218 Bulk differences in low-level updraft strength and vertical vorticity imply that the two VOR-
219 TEX2 composite soundings do indeed contain sufficiently distinct ingredients to “correctly” sim-
220 ulate nontornadic and tornadic supercells, which is rather remarkable. The subsequent goals of
221 this study are to document and explain the processes that lead to these storm-scale differences
222 and then establish how those processes are directly linked to the corresponding environments. To
223 do this, we will explore the basic chronology of each supercell individually, starting with the tor-

⁵The vortex that develops from $t \approx 15 - 35 \text{ min}$ is induced by the updraft nudging convection initiation, and compensating subsidence (similar to Parker 2012), combined with Coriolis force on the perturbation winds, and hence not the subject of the forthcoming analysis. Although vortices prior to the arrival of cool surface outflow have recently been evaluated by Markowski (2016) and Roberts et al. (2016), it is uncertain if these are relevant to real convective storms. Interestingly, although equal updraft forcing and Coriolis acceleration was applied in both simulations, the early near-surface vortex is much more intense in the simulation initialized with the tornadic VORTEX2 environment containing near-surface streamwise horizontal vorticity.

⁶To accurately depict a tornado, grid spacing an order magnitude higher ($\Delta x \approx 10 \text{ m}$) and a more complete understanding of tornado boundary layers is required (Rotunno 2013).

224 nadic supercell, then return to more specific comparisons related to the processes that result in
225 tornadogenesis (or the lack thereof) in Section 4.

226 *c. Tornadic supercell*

227 The cyclonically rotating right-mover exhibits supercellular structures by $t = 40$ min in the
228 tornadic simulation (Fig. 3b). A hook echo begins to form at approximately $t = 45$ min (Fig.
229 6). At this time, the mid-level updraft is directly above the intersection of the rear and forward
230 flank outflow boundaries (Figs. 3c, 6a,c), where widespread values of subtornadic surface vertical
231 vorticity can be found (Fig. 6d). The low-level updraft already exceeds 25 m s^{-1} and a broad area
232 of ascent greater than 10 m s^{-1} exists throughout the weak-echo region (Fig. 6b).

233 An elongated zone of surface vertical vorticity, extending toward the rear-flank outflow
234 boundary from the forward flank precipitation region of the supercell, develops just prior to t
235 = 40 minutes (visible at $t = 45$ min in Fig. 6d). Because this zone has both cyclonic shear vorticity
236 and air parcels moving parallel to the corridor, we will refer to this as a vorticity river, consistent
237 with the terminology of Dahl et al. (2014). As the supercell evolves, this vorticity river feeds high
238 vorticity air parcels into the tornado (Fig. 7,8). Other studies, through both observations and sim-
239 ulations, have referred to similar phenomena as vorticity feeders (Fujita et al. 1976, see their Fig.
240 25), vortex sheets (e.g. Markowski et al. 2014), left-flank convergence boundaries (Beck and Weiss
241 2013)⁷, or just shear boundaries (Brandes 1978, see their Fig. 18). At $t = 45$ min, the vorticity
242 river is characterized by vertical vorticity of 0.02 s^{-1} near the surface (Fig. 6d), and is associated
243 with a gradient in density potential temperature (Fig. 6c), localized confluent horizontal velocity
244 field (Fig. 6c), and streamwise horizontal vorticity vectors (Fig. 6d), much like those discussed by
245 Dahl et al. (2014).

⁷The vorticity rivers are focused along the left-flank convergence boundary. Beck and Weiss (2013) did not specifically explore vorticity.

During the 15 minutes prior to tornadogenesis in the tornadic supercell, the low-level mesocyclone dramatically strengthens. The core of the updraft begins to extend towards lower levels, with maximum velocities at 1 km increasing from 20 to 55 m/s, and the mesocyclone aloft rapidly intensifies (Figs. 4, 5, 9a - c). A distinct curl to the hook echo begins to develop from $t = 45 - 55$ min (Fig. 7a), along with the main downdraft to the northwest of the hook echo also intensifying (Fig. 7b). After the extended period of low-level mesocyclone intensification, an intense tornado develops at $t = 55$ min, rapidly increasing from surface vertical vorticity values of 0.2 s^{-1} to values greater than 1.1 s^{-1} at $t = 60$ min (Figs. 8,9d). The approximately 15 min timescale for the development of tornadic strength vorticity is consistent with scale analysis presented in Davies-Jones et al. (2001). The maximum pressure drop at the surface is approximately 40 hPa; this is associated with a maximum 10 m wind speed near 70 m s^{-1} . The tornado forms at the inflection point between rear-flank outflow boundary and the vorticity river (Fig. 7c). Even though the low-level mesocyclone is strengthening aloft prior to tornadogenesis, vorticity at the surface develops independently of the circulation aloft and then rapidly builds upward within the lowest few hundred meters, eventually coupling with (and further intensifying) the low-level mesocyclone. This process is consistent with the mode II tornadogenesis process from Trapp and Davies-Jones (1997) and Davies-Jones et al. (2001) and has many similarities to the evolution of the low-level mesocyclone and resulting tornado in the Goshen County supercell (the most significant tornado in the V2 composite dataset; Markowski et al. 2012b; French et al. 2013).

The vorticity river has rotated into a north/south orientation near tornadogenesis time (Figs. 7d, 9e). It remains in a quasi-north/south orientation for approximately 10 min during the most intense phase of the tornado (Fig. 8d). During the intensification phase, the difference in density potential temperature across the vorticity river is approximately 1 K km^{-1} , with colder density potential temperature to its west (i.e. $\nabla \theta_p$ points from west to east implying baroclinic generation

270 of streamwise vorticity as in Davies-Jones and Brooks 1993, Fig. 7c). Air with highly streamwise
271 horizontal vorticity (plus appreciable vertical vorticity) appears to flow through the vorticity river
272 and then curves cyclonically into the tornado (Fig. 7d). The tornado maintains a nearly constant
273 storm-relative position during peak intensity (Fig. 8c). Beginning at $t = 60$ min, strong descent
274 emerges towards the back of edge the hook echo (Fig. 8b), which is accompanied with positive
275 density potential temperature perturbations at the surface embedded within the hook echo (Fig.
276 8c). By $t = 65$ min (not shown), the vorticity river becomes detached from the tornado following
277 strong divergence near the tornado's axis of rotation, reducing the convergence of vertical vorticity
278 (Rasmussen and Straka 2007). Downward velocities exceed -20 m s^{-1} at 200 m above the surface.
279 At this point, the vortex begins rotating cyclonically around the mesocyclone. It briefly weakens
280 at $t = 72$ min before strengthening again by $t = 75$ min. The vortex has been displaced towards the
281 rear of the storm, far removed (more than 5 km) from the outflow/inflow interface (Fig. 10a,c).
282 The mid-level mesocyclone has begun to cycle with a new updraft developing downshear (Fig. 3i),
283 while the old mesocyclone moves toward the rear of the storm. An anticyclonic tornado develops
284 underneath a low-level mesoanticyclone within the supercell's flanking line as the old updraft
285 occludes towards the rear of the storm and a new updraft develops downshear (Fig. 10c; similar to
286 Bluestein et al. 2016) and lasts just over 10 min, with a maximum 10 m wind speed near 35 m s^{-1} .
287 Both tornadoes ultimately dissipate near $t = 80$ min following the emergence of colder outflow,
288 with density potential temperature perturbation exceeding -4 K in the hook echo, shunting the
289 vortices away from the weakening low-level updraft (Figs. 9g,h, 10c).

290 The new updraft never intensifies to the degree the previous one did, and the supercell cycles
291 twice more during the remainder of the simulation, remaining disorganized at low-levels. Near the
292 end of the 2 hr simulation, the supercell once again begins to take on several features that were
293 previously seen during the subtornadic phase documented above, including a vorticity river in the

294 forward flank precipitation and an intensifying low-level updraft. However, because we wished
295 to focus on differences in the early evolution of the tornadic versus the nontornadic storms, the
296 simulation was not extended beyond 2 h.

297 *d. Nontornadic supercell*

298 Following initiation in the nontornadic simulation, the developing storm remains disorga-
299 nized in the low-levels until $t = 50$ min when supercellular features become more apparent (Fig.
300 2d). At $t = 60$ min, the mid-level updraft is several kilometers ahead of the near-surface precip-
301 itation (Fig. 2f). While vertical velocities exceeding 15 m s^{-1} are present at 1 km (Fig. 11b),
302 the low-level updraft is generally disorganized compared to the tornadic supercell's 1 km updraft,
303 with pockets of descent present in the weak-echo region (Fig. 11b). The main downdraft region to
304 the northwest of the low-level updraft has begun to intensify, with velocities and density potential
305 temperature perturbations exceeding -20 m s^{-1} and -5 K respectively (Fig. 11b,c). Widespread
306 subtornadic surface vertical vorticity is already present within the rear-flank outflow, and as in the
307 tornadic supercell, the vertical vorticity appears to emerge from vorticity rivers, which approach
308 from the main precipitation core to the north (Fig. 11a,d). These vorticity rivers are again associ-
309 ated with localized confluence and a $1 - 2 \text{ K}$ cross-river difference in density potential temperature
310 perturbation. Many such vorticity rivers emanate from the pulsing main downdraft area throughout
311 the supercell's most intense phase; however, none of these vorticity rivers acquire a quasi-steady
312 storm-relative position in the way seen in the tornadic supercell (Figs. 11, 12, 13). This might
313 shorten the time window within which the conditions for tornadogenesis coexist.

314 The supercell develops a hook echo by $t = 65$ min and produces a short-lived, broad, shallow
315 vortex near $t = 70$ min (Fig. 12). The near-surface vortex forms several kilometers west of the
316 main low-level updraft (Fig. 12b,d), deeply embedded in the rear-flank outflow. The vortex briefly

317 develops a peak intensity of surface vertical vorticity of 0.25 s^{-1} , with a pressure drop of 5 hPa and
318 a maximum instantaneous, storm-relative surface wind speed of near 27 m s^{-1} . This represents
319 the closest attempt at tornadogenesis during the nontornadic VORTEX2 simulation⁸. The broad
320 vortex never contracts into a tornado and quickly dissipates into the rear-flank outflow.

321 Preceding the vortex development, the low- and mid-level updraft strengthen. However,
322 due to the intensifying near-surface vortex, an “occlusion-like” downdraft forms. The occlusion
323 downdraft (Klemp and Rotunno 1983) is a dynamical symptom of lower perturbation pressure at
324 the surface than aloft, normally induced by increasing rotation near the surface. It is most-often
325 discussed within tornadic supercells (e.g. Markowski 2002), although Wakimoto and Cai (2000)
326 showed that occlusion downdrafts can form in nontornadic supercells as well. In the nontor-
327 nadic VORTEX2 supercell simulation, this downdraft disrupts the developing vortex by replacing
328 a concentrated area of convergence with divergence. The result is an annular region of vertical
329 vorticity surrounding the downdraft (Fig. 12d), instead of a compact vortex, such as produced by
330 the tornadic supercell. The broad, near-surface circulation is even evident in the density poten-
331 tial temperature perturbation field ahead of the hook echo (Fig. 12c). Warmer temperature near
332 the center of the circulation is associated with the dynamically-induced downdraft and attendant
333 adiabatic warming.

334 By $t = 80 \text{ min}$, the low-level updraft has taken on a horseshoe-shaped structure, with more
335 precipitation present in the vicinity of the hook echo (Fig. 13). Despite density potential tempera-
336 ture perturbations of only -1 to -3 K (Fig. 13c), the supercell appears to be “outflow-dominated”,
337 exhibiting an increase in precipitation within the hook echo and a “bowed-out”, narrow low-level
338 updraft along the rear-flank outflow boundary (Fig. 13b). Ample surface vorticity is still present in

8 A few other brief spin-ups occur during the simulation along the rear-flank gust front and towards the back edge of the hook echo. Due to their location, these shallow spin-ups (< 250 m in depth) were considered more like “gustnadoes” rather than failed tornadogenesis.

339 the hook echo (Fig. 13d); however it is displaced rearward from the strong low-level updraft (Fig.
340 13b), and thus it is not amplified by stretching. Meanwhile, dynamically-induced downdrafts con-
341 tinue to form in the vicinity, preventing sustained convergence where subtornadic values of vertical
342 vorticity are present (Fig. 12b). An explanation for the development of the dynamically-induced
343 downdrafts will be explored further in Section 4.

344 Following this period of activity, the low-level mesocyclone, which had been relatively per-
345 sistent for the prior 30 minutes, occludes toward the rear of the storm. The supercell goes onto
346 cycle once more during the remainder of the simulation, but never again comes close to producing
347 a tornado.

348 **4. Storm-scale differences contributing to tornadogenesis or tornadogenesis failure**

349 To further illustrate differences between the two supercells, time composites centered on
350 the mid-level updraft were created for the 15 minutes during the failed genesis in the nontornadic
351 supercell and the 15 minutes leading up to the most intense near-surface vortex in the tornadic
352 supercell. In the nontornadic supercell, the main updraft is ahead of the precipitation and overall
353 weaker (Fig. 14a). The tornadic supercell has a stronger updraft immediately adjacent to the
354 hook echo (Fig. 14b). Both simulations produce large values of surface vorticity; however the
355 nontornadic supercell produces an overabundance of surface vorticity behind the updraft, nearer
356 to the precipitation (Fig. 14c,d). Without being superimposed under the low-level updraft, the
357 surface vorticity that does develop in the nontornadic supercell is not stretched into a deep, intense
358 vortex. Instead a persistent downdraft signal is present near the surface vorticity in the nontornadic
359 supercell (Fig. 14a,c), likely a dynamical response to the rotation at the surface. Also, a stronger
360 signal for descent is present in the rear of the storm (Fig. 14a) and higher concentrations of
361 precipitation mixing ratio within the hook echo of the nontornadic supercell (not shown). The

362 outflow temperature in the rear-flank is not noticeably different between the simulations (Fig.
363 14e,f). On average, both storms have peak density potential temperature perturbations near -7 K
364 during the 15 minute time composite. The forward-flank baroclinic gradient north of the low-
365 level updraft is slightly stronger (~ 1 K) in the tornadic supercell (Fig. 14e,f). The orientation of
366 the storm-relative cold pool is slightly shifted, likely because ambient low-level winds are from
367 the east in the nontornadic case and from the southeast in the tornadic case. Although both cold
368 pools have similar potential temperature deficits, the outflow boundary in the nontornadic supercell
369 extends farther ahead of the rear-flank precipitation, and the low-level updraft appears bowed out
370 along the rear-flank outflow boundary (Fig. 14e,f).

371 In order to more clearly visualize the tornadogenesis failure mode and successful tornadoge-
372 nesis process in the respective supercells, parcels were launched in a $20 \times 20 \text{ km}^2$ box surrounding
373 the developing surface vorticity every 62.5 m in the horizontal and every 20 m in the lowest 2 km
374 at $t = 50 \text{ min}$ ($t = 60 \text{ min}$) in the tornadic (nontornadic) supercell. In total, nearly 13 million parcels
375 was integrated forward⁹ on each model time step (0.6 s) for 10 min, with output saved every 10 s.
376 Parcel that acquired vertical vorticity near the surface in the nontornadic supercell fail to be lifted
377 and stretched into the overlying storm (Fig. 15a). The few parcels that did begin to rise experience
378 abrupt descent back towards the surface. Since the outflow region is not particularly cold relative
379 to the ambient inflow air, the failure of parcels to be lifted into the storm is most likely due to
380 the lack of a broad, consistent area of dynamic lifting (shown later). Additionally, cross-sections
381 through developing vortices show a quick transition from an "in-up" to a "down-out" circulation
382 (not shown), as in the nontornadic supercells analyzed by Markowski et al. (2011). No such issue
383 exists in the tornadic supercell; parcels that acquire large surface vertical vorticity traverse down

⁹In highly curved, confluent flow regimes, Dahl et al. (2012) showed that forward trajectories with small time steps are more accurate than backward trajectories.

384 the vorticity river within an east-west baroclinic gradient before curling cyclonically into the tor-
385 nado and swiftly rising into the low-level mesocyclone (Fig. 15b). Since the tornado is on the
386 eastern edge of the low-level updraft (Fig. 7b,c), some of the parcels rise briefly to the west before
387 descending back down towards the surface as they curl into the tornado. The rapid ascent of the
388 parcels into the mesocyclone indicates a coupling between the surface circulation and the over-
389 lying updraft, a configuration highly supportive of vortex stretching. The opposite is true in the
390 nontornadic supercell; the surface circulation appears decoupled from the low-level updraft, lead-
391 ing to a disruption of vortex stretching and thus tornadogenesis failure (Trapp 1999; Markowski
392 et al. 2011).

393 The pretornadic intensification of the low-level updraft in the tornadic supercell is caused by
394 an increase in the dynamic vertical perturbation pressure gradient acceleration¹⁰. The low-level
395 dynamic vertical accelerations increase by 300% in the 15 minutes prior to tornadogenesis ($t = 40$
396 - 55 min; Fig. 16 top left). The apex in 0 - 1 km dynamic vertical perturbation pressure gradient
397 acceleration occurs at the same time the tornado peaks in intensity¹¹. The 0 - 3 km dynamic vertical
398 perturbation pressure gradient acceleration also shows large increases but not until 10 minutes later
399 ($t = 50$ min; Fig. 16 top right). The nontornadic supercell has much weaker increases in the 0 - 1
400 and 0 - 3 km dynamic vertical perturbation pressure gradient acceleration during its failed genesis
401 period ($t = 60$ - 75 min; Fig. 16 top), and these accelerations are not spatially superimposed over
402 the surface subtornadic vertical vorticity for a prolonged period of time.

¹⁰Our decomposition of the perturbation pressure components and the corresponding vertical accelerations are described in Section 3b of Coffer and Parker (2015).

¹¹The substantial increases in upward dynamic vertical perturbation pressure gradient acceleration are not simply a symptom of the developing tornado but rather the catalyst. Strong rotation at the surface, as in a tornado, would instead be associated with a *downward-directed* dynamic vertical perturbation pressure gradient acceleration.

403 The main, persistent area of lifting in the nontornadic supercell is several kilometers ahead
404 of where the surface vorticity resides (cf. Figs. 14c, 17a-c). Behind this, the dynamic acceleration
405 is strikingly disorganized as both positive and negative areas of acceleration frequently form and
406 dissipate (Fig. 17a-c). Without a persistent area of upward lifting, the surface vorticity that does
407 develop in the nontornadic supercell is not likely to be contracted into a tornado. In contrast, the
408 tornadic supercell has a sustained area of upward accelerations encompassing the entire weak-echo
409 region where the tornado will eventually form (Fig. 17d,e). Interestingly, at the time the tornado
410 finally dissipates (Fig. 17f), the acceleration field looks as disorganized as the nontornadic storm
411 did throughout its entire life cycle.

412 It is noteworthy that the surface circulation¹² in the tornadic case is very similar to that in
413 the nontornadic case during the key time period (Fig. 16 bottom panels), indicating that enough
414 surface circulation exists in the nontornadic supercell (Fig. 18a-c) to be tornadic if air parcels
415 could be converged to a sufficient radius. However, the surface circulation equals or exceeds the
416 circulation at 1 km in the nontornadic supercell (Fig. 16 bottom left). Meanwhile, in the tornadic
417 supercell, the 1 km circulation is much stronger than the surface circulation (Fig. 16 bottom right).

418 In addition to a higher magnitude of circulation aloft in the tornadic supercell, the two su-
419 percells have contrasting orientations of cyclonic/anticyclonic circulation at 1 km (cf. Figs. 18d-
420 f,19d-f). The 1 km AGL circulation in the nontornadic storm is mainly found behind the main
421 updraft region and has a higher deformation component to the wind field, rather than a closed
422 rotational circulation (Fig. 18d-f). Deformation is associated with locally positive nonlinear dy-
423 namic pressure perturbations (Markowski and Richardson 2010, p. 30), explaining the positive
424 nonlinear dynamic pressure perturbations at 1 km in the nontornadic supercell (Fig. 18d-f). This

¹²Circulation (C) is defined as the area (A) sum of vertical vorticity (ζ), i.e. $\iint_A \zeta dA$. Herein, circulation was computed within a 1-km-radius horizontal ring centered at each grid point within the domain's constant grid spacing inner mesh.

leads to a dearth of vertical vorticity stretching at the surface because the dynamic vertical pressure perturbation gradient acceleration is negligible, or even downward (Fig. 17a-c). The lack of persistent dynamic lifting, in combination with the surface circulation exceeding the circulation at 1 km AGL, supports the assumption in Section 3d that dynamically-induced downdrafts disrupted the vortex spin-up in the nontornadic supercell, ultimately leading to a failed tornadogenesis attempt. A similar disassociation between the updraft and circulation of the mesocyclone at 1 km AGL, in addition to a large deformation component to the flow, was noted in an observed nontornadic supercell with predominately near-surface crosswise horizontal vorticity analyzed by Beck et al. (2006). Meanwhile, in the tornadic supercell, a clear low-level closed circulation exists in the tornadic supercell at 1 km and is collocated with the updraft (Fig. 19d-f). The closed circulation leads to negative nonlinear dynamic pressure perturbations in the mesocyclone (Fig. 19d-f) and results in a much more favorable setup for upward dynamic accelerations (Fig. 17d-f). The main, cyclonic tornado develops directly underneath the vertically stacked low-level mesocyclone (Fig. 19b,e). The strong circulation aloft, and the associated areas of lower nonlinear dynamic pressure perturbations, in the tornadic supercell provide a broad, consistent area of upward dynamic acceleration that mitigates the effect of dynamically-induced downdrafts as the vorticity is intensifying at the surface.

The differences in the orientation of the 1 km circulation couplets in the nontornadic and tornadic supercells likely result from the varying flux of streamwise horizontal vorticity into the nontornadic vs tornadic updrafts. As described by Davies-Jones (1984), the tilting and advection of crosswise horizontal vorticity by the storm-relative wind engenders positive/negative circulation couplets on either side of the updraft maximum, whereas streamwise horizontal vorticity results in the positive circulation component being advected preferentially into the updraft. To quantitatively evaluate the bulk characteristics of the low-level mesocyclone in each supercell, another set of

449 parcels were launched at every horizontal grid point and every 20 m vertically in the lowest 2
450 km AGL of the inflow region at 10 minutes prior to the time period composited in Figure 14.
451 Trajectories were filtered to isolate the 500 parcels that acquired the largest vertical velocity (with
452 at least 0.01 s^{-1} of vertical vorticity) within 50 m of 1 km AGL. All parcels that entered the low-
453 level mesocyclone originated below 300 m AGL. The horizontal vorticity in this near-surface layer
454 was predominately crosswise (streamwise) in the nontornadic (tornadic) environment (Fig. 20).
455 Not surprisingly, these low-level mesocyclone parcels also had a much higher vertical velocity
456 and obtained much larger values of vertical vorticity in the tornadic supercell (Fig. 20). This
457 suggests that not only does larger low-level shear establish the base of the mesocyclone at lower
458 altitudes (as suggested by Markowski et al. 2012b; Markowski and Richardson 2014; Coffer and
459 Parker 2015), but predominately crosswise vorticity in the boundary layer leads to a less favorable
460 configuration of the low-level mesocyclone for tornadogenesis (cf. Fig. 18,19).

461 **5. Idealized updrafts in VORTEX2 wind profiles**

462 It is clear that the composite VORTEX2 environments contain sufficient information to "cor-
463 rectly" produce supercells with nontornadic and tornadic characteristics. The failure mode for
464 tornadogenesis in the nontornadic supercell appears to be due to a disorganized low-level meso-
465 cyclone and thus a lack of convergence and stretching of subtornadic vorticity into a tornado.
466 However, direct attribution of this process to the environmental profiles is difficult to completely
467 ascertain from the full-physics simulations. In Section 4, we inferred that the low-level crosswise
468 horizontal vorticity in the nontornadic environment, when tilted by the supercell's updraft, yields
469 an unfavorable couplet of cyclonic and anticyclonic circulation, with neither collocated with the
470 updraft. This might explain the less steady updraft in the nontornadic supercell, as well as its
471 displacement from the zone of large surface vorticity. In order to isolate the direct effect of dif-

472 differences in the VORTEX2 low-level wind profiles upon developing updrafts, additional simpler
473 simulations were conducted.

474 In a similar manner to Markowski and Richardson (2014), a stationary, cylindrical heat
475 source is implemented by adding a heating tendency to the model's potential temperature equa-
476 tion. This forcing has a peak amplitude of 0.05 K s^{-1} ("equivalent" to 0.5 m s^{-2} accumulated
477 parcel buoyancy), varies as the cosine of distance from its center at 5.25 km above the origin, and
478 has a horizontal and vertical radii of 3 and 4.75 km, respectively. The size, shape, and magnitude
479 of the heating tendency emulates the latent heat release in a supercell's updraft. These simulations
480 are run dry with a grid spacing of 500 m on a domain of $100 \times 100 \times 18 \text{ km}^3$. The environmen-
481 tal thermodynamic profile has a constant potential temperature of 300 K up to 12 km, where a
482 potential temperature inversion of 20 K km^{-1} was added to emulate the tropopause. Otherwise,
483 the model configuration, including the VORTEX2 wind profiles, is identical to the full-physics
484 simulations discussed previously. All differences between the idealized nontornadic and tornadic
485 simulations discussed below are *solely due to the wind profile*.

486 Both idealized simulations acquire an approximately steady mid-level updraft and meso-
487 cyclone by 20 min. The nontornadic simulation has a maximum vertical velocity of 64 m s^{-1}
488 (similar to the full physics nontornadic VORTEX2 simulation) and maximum vertical vorticity at
489 3 km AGL of 0.036 s^{-1} . The tornadic simulation has a weaker upper-level updraft (54 m s^{-1})
490 but similar values of mid-level mesocyclonic vorticity values. The weaker updraft aloft in the tor-
491 nadic profile, despite identical forcing, is likely due to a more tilted updraft caused by its higher
492 deep-layer shear. A positive feedback loop exists within the simulations. Tilting of horizontal
493 vorticity into the vertical by the updraft leads to rotationally induced pressure falls at mid-levels,
494 which enhances the dynamic lifting by the updraft, thus leading to a stronger updraft (and more
495 tilting at lower altitudes). This feedback eventually generates vertical velocities in excess of 10

496 m s^{-1} in the lowest kilometer in both simulations. Many similarities exist in the circulation field
497 between the idealized and full-physics simulations (cf. Figs. 18, 19, 21). The 1 km circula-
498 tion is rapidly intensifying by $t = 40$ min in the tornadic idealized simulations (Fig. 21d-f), near
499 the time when the low-level mesocyclone intensifies in the full-physics tornadic simulation. The
500 low-level circulation is stronger in the tornadic simulation than the nontornadic simulation and is
501 more strongly correlated with the low-level updraft (Fig. 21). Just as in the full-physics tornadic
502 supercell, the stronger low-level updraft is driven by a stronger upward directed dynamic pertur-
503 bation pressure gradient acceleration (Fig. 22) as the updraft aloft acquires rotation by ingesting
504 storm-relative helicity from the near-surface layer. In contrast, the low-level mesocyclone in the
505 nontornadic simulation is characterized by a positive/negative circulation couplet not collocated
506 with the intensifying low-level updraft (Fig. 21a-c).

507 Bulk characteristics of the low-level mesocyclone in the idealized simulations are evaluated
508 through trajectories. With a focus on the low-level mesocyclone during the last 10 minutes of the
509 simulations, only the trajectories that acquired vertical velocity of 10 m s^{-1} and positive vertical
510 vorticity near 1 km were analyzed. Over twice as many parcels met these criteria in the tornadic
511 simulation than the nontornadic (5398 vs. 2024). All parcels that entered the low-level mesocy-
512 clone originated below 530 m AGL, and the median initial height of the parcels was 270 m and
513 110 m AGL in the nontornadic and tornadic simulation, respectively. As in the full-physics simu-
514 lations, parcels that ended up in the low-level mesocyclone have much larger values of streamwise
515 horizontal vorticity, and in spite of identical updraft forcing, they experienced higher vertical ve-
516 locities and obtained much larger values of vertical vorticity due to more intense stretching (Fig.
517 23).

518 These idealized simulations capture the first order interactions between the wind profile and
519 the updraft. Even in a dry adiabatic environment with identical updraft forcing, the wind profile

drives unambiguous low-level mesocyclone differences. Thus, in these VORTEX2 composite profiles, the general storm structure, as well as the storm's potential to contract the abundant subtornadic vorticity into a tornado, seems to be predominantly governed by the low-level environment wind profile. Primarily crosswise vorticity near the surface favors a low-level mesocyclone located primarily in a shear zone behind the updraft, rather than a closed circulation collocated with the updraft. This deformation does not allow the mesocyclone to develop the pressure falls needed for intense dynamic lifting at low-levels. In the full-physics simulations, the lack of a mitigating upward-directed vertical perturbation pressure gradient in the nontornadic supercell causes occlusion downdrafts whenever large surface vorticity develops, preventing the incipient vortex from fully contracting into a tornado.

6. Synthesis

a. Summary

In this article, we investigated the storm-scale differences between nontornadic and tornadic supercell simulations initialized with the composite VORTEX2 environments. Both the nontornadic and tornadic environments would generally be considered favorable for supercells and tornadoes, with sufficiently large CAPE, modest CIN, low LCLs, and ample deep-layer and low-level shear. While our understanding of environments that favor tornadic versus nontornadic storms has progressed in recent years, it is still unclear how these factors influence the in-storm processes that result in the final steps of the tornadogenesis process. Observations of nontornadic supercells show remarkable similarity to their tornadic counterparts, and simulations have demonstrated that it is rather easy to generate subtornadic-strength surface vertical vorticity in supercells. With these

541 considerations in mind, revisiting the research questions outlined in Section 1, our simulations
542 show the following:

543 1. Do the two VORTEX2 composite soundings contain sufficiently distinct ingredients to “cor-
544 rectly” simulate nontornadic and tornadic supercells in the respective nontornadic and tor-
545 nadic environments?

- 546
- 547 • Simulations in both the nontornadic and tornadic environments produce a strong super-
548 cell with a robust mid-level mesocyclone, updraft, and a hook echo reflectivity structure
549 at low altitudes. However, the low-level updraft is much more intense in the tornadic
550 supercell. The tornadic supercell develops an intense, long-lasting tornado, reaching
551 high-end EF3 wind speeds and lasting for approximately 25 min. The nontornadic su-
552 percell only produces shallow vortices that are transient in nature, never reaching the
553 EF0 wind speed threshold. Therefore, even though the differences between the two en-
554 vironments are rather subtle, it does seem like that they contain specific ingredients that
may discriminate between nontornadic and tornadic supercells.

555 2. What is the failure point for tornadogenesis in the nontornadic supercell compared to the
556 tornadic supercell?

- 557
- 558 • The nontornadic supercell readily produces subtornadic values of vertical vorticity at
559 the surface; however, these vortices fail to attain tornadic intensity due to a lack of
560 convergence and stretching by the low-level updraft. A disorganized low-level mesocy-
561 clone, with no significant dynamic pressure falls, leads to insufficient dynamic lifting
562 and stretching of parcels that acquire with surface vertical vorticity. This failure mode
563 occurs despite only weakly negative buoyancy in the rear-flank outflow. During the clos-
est attempt at tornadogenesis in the nontornadic supercell, a strong downdraft develops

564 near the axis of rotation, likely due to the circulation at the surface exceeding the circu-
565 lation aloft in the low-level mesocyclone. This “occlusion-like” downdraft disrupts the
566 developing vortex by inducing near-surface divergence.

567 3. Can this failure point be specifically traced to some trait that differs between the nontornadic
568 and tornadic environments?

- 569
- 570 • The disorganized low-level mesocyclone and lack of dynamic lifting in the nontornadic
571 supercell appears to be linked to predominately crosswise vorticity in the lowest few
572 hundred meters in the nontornadic environment. The nontornadic low-level mesocy-
573 clone is characterized by a cyclonic/anticyclonic circulation couplet not collocated with
574 the low-level updraft, a symptom of fluxing horizontal vortex lines with a substantial
575 crosswise component into and through the updraft (Fig. 24a). Without the collocation
576 of the updraft and vertical vorticity maximum, the nontornadic supercell does not have
577 a broad, consistent upward-directed vertical perturbation pressure gradient to stretch
578 subtornadic surface vortices into a tornado and to mitigate the downward-directed dy-
579 namical accelerations associated with these developing vortices. No such issue exists
580 in the tornadic supercell, as large 0 - 500 m streamwise horizontal vorticity is ingested
581 by the updraft, leading to a high correlation between the updraft and low-level mesocy-
582 clone circulation (Fig. 24b). This results in dynamic perturbation pressure falls within
583 the low-level updraft and strong dynamic lifting to stretch high vertical vorticity parcels
at the surface into a tornado.

584 *b. Future work*

585 Although these simulations utilized the VORTEX2 composite environments directly from
586 Parker (2014), low- and mid-level wind profile and thermodynamic profile sensitivity tests are
587 ongoing to systematically study the subtle differences between the nontornadic and tornadic en-
588 vironments. Another interesting avenue for future analysis of these simulations includes more
589 detailed vorticity budgets (e.g. tracking the barotropic, baroclinic, and/or viscous components of
590 surface vertical vorticity generation during the creation and intensification of subtornadic surface
591 vorticity; Dahl et al. 2014; Markowski 2016). Such simulations might gain added realism through
592 radar data assimilation techniques (e.g. Snyder and Zhang 2003; Dowell et al. 2004; Marquis et al.
593 2014). For this reason, simulations of two VORTEX2 cases, one nontornadic and one tornadic,
594 are planned to investigate whether similar updraft and circulation features to those reported herein
595 exist in less idealized simulations with contrasting magnitudes of low-level streamwise horizontal
596 vorticity.

597 *Acknowledgments.* This research was supported by NSF Grants AGS-1156123 and AGS-
598 1359709. We especially thank Dr. George Bryan for his ongoing support of CM1. Dr. Johannes
599 Dahl is acknowledged for sharing his parcel interpolation/identification code, as well as insightful
600 discussion on minimizing friction with the Coriolis force. We also thank the anonymous reviewers
601 who are currently reading this manuscript. The first author's committee members, Drs. Gary Lack-
602 mann, Sandra Yuter, Johannes Dahl, and Lou Wicker, as well as members of the NCSU Convective
603 Storms group, provided helpful feedback on an earlier version of this manuscript.

604 **References**

- 605 Adlerman, E. J., K. K. Droegemeier, and R. Davies-Jones, 1999: A numerical simulation of cyclic
606 mesocyclogenesis. *J. Atmos. Sci.*, **56** (13), 2045–2069.
- 607 Beck, J., and C. Weiss, 2013: An assessment of low-level baroclinity and vorticity within a simu-
608 lated supercell. *Mon. Wea. Rev.*, **141** (2), 649–669.
- 609 Beck, J. R., J. L. Schroeder, and J. M. Wurman, 2006: High-resolution dual-doppler analyses of
610 the 29 may 2001 kress, texas, cyclic supercell. *Mon. Wea. Rev.*, **134** (11), 3125–3148.
- 611 Bluestein, H. B., M. M. French, J. C. Snyder, and J. B. Houser, 2016: Doppler radar observations
612 of anticyclonic tornadoes in cyclonically rotating, right-moving supercells. *Mon. Wea. Rev.*,
613 **144** (4), 1591–1616.
- 614 Brandes, E. A., 1978: Mesocyclone evolution and tornadogenesis: Some observations. *Mon. Wea.*
615 *Rev.*, **106** (7), 995–1011.
- 616 Brotzge, J., S. Erickson, and H. Brooks, 2011: A 5-yr climatology of tornado false alarms. *Wea.*
617 *Forecasting*, **26** (4), 534–544.
- 618 Bryan, G. H., and H. Morrison, 2012: Sensitivity of a simulated squall line to horizontal resolution
619 and parameterization of microphysics. *Mon. Wea. Rev.*, **140** (1), 202–225.
- 620 Bunkers, M. J., B. A. Klimowski, J. W. Zeitler, R. L. Thompson, and M. L. Weisman, 2000:
621 Predicting supercell motion using a new hodograph technique. *Wea. Forecasting*, **15** (1), 61–79.
- 622 Coffer, B. E., and M. D. Parker, 2015: Impacts of increasing low-level shear on supercells during
623 the early evening transition. *Mon. Wea. Rev.*, **143** (5), 1945–1969.

- 624 Craven, J. P., H. E. Brooks, and J. A. Hart, 2004: Baseline climatology of sounding derived
625 parameters associated with deep, moist convection. *Natl. Weather Dig.*, **28** (1), 13–24.
- 626 Dahl, J. M., 2015: Near-ground rotation in simulated supercells: On the robustness of the baro-
627 clinic mechanism. *Mon. Wea. Rev.*, **143** (12), 4929–4942.
- 628 Dahl, J. M., M. D. Parker, and L. J. Wicker, 2012: Uncertainties in trajectory calculations within
629 near-surface mesocyclones of simulated supercells. *Mon. Wea. Rev.*, **140** (9), 2959–2966.
- 630 Dahl, J. M., M. D. Parker, and L. J. Wicker, 2014: Imported and storm-generated near-ground
631 vertical vorticity in a simulated supercell. *J. Atmos. Sci.*, **71** (8), 3027–3051.
- 632 Davies-Jones, R., 1982: Observational and theoretical aspects of tornadogenesis. *Intense Atmo-*
633 *spheric Vortices*, Springer, 175–189.
- 634 Davies-Jones, R., 1984: Streamwise vorticity: The origin of updraft rotation in supercell storms.
635 *J. Atmos. Sci.*, **41** (20), 2991–3006.
- 636 Davies-Jones, R., 2015: A review of supercell and tornado dynamics. *Atmos. Res.*, **158–159**, 274–
637 291.
- 638 Davies-Jones, R., and H. Brooks, 1993: Mesocyclogenesis from a theoretical perspective. *The*
639 *Tornado: Its Structure, Dynamics, Prediction, and Hazards*, 105–114.
- 640 Davies-Jones, R., R. J. Trapp, and H. B. Bluestein, 2001: Tornadoes and tornadic storms. *Severe*
641 *Convective Storms*, Springer, 167–221.
- 642 Deardorff, J. W., 1980: Stratocumulus-capped mixed layers derived from a three-dimensional
643 model. *Bound.-Layer Meteor.*, **18** (4), 495–527.

- 644 Dowell, D. C., F. Zhang, L. J. Wicker, C. Snyder, and N. A. Crook, 2004: Wind and temperature
645 retrievals in the 17 may 1981 arcadia, oklahoma, supercell: Ensemble kalman filter experiments.
646 *Mon. Wea. Rev.*, **132** (8), 1982–2005.
- 647 Esterheld, J. M., and D. J. Giuliano, 2008: Discriminating between tornadic and non-tornadic
648 supercells: A new hodograph technique. *Electronic J. Severe Storms Meteor.*, **3** (2).
- 649 Frame, J., and P. Markowski, 2010: Numerical simulations of radiative cooling beneath the anvils
650 of supercell thunderstorms. *Mon. Wea. Rev.*, **138** (8), 3024–3047.
- 651 French, M. M., H. B. Bluestein, I. PopStefanija, C. A. Baldi, and R. T. Bluth, 2013: Reexamining
652 the vertical development of tornadic vortex signatures in supercells. *Mon. Wea. Rev.*, **141** (12),
653 4576–4601.
- 654 Fujita, T. T., G. S. Forbes, and T. A. Umenhofer, 1976: Close-up view of 20 march 1976 tornadoes:
655 Sinking cloud tops to suction vortices. *Weatherwise*, **29** (3), 116–145.
- 656 Halbert, K., W. Blumberg, and P. Marsh, 2015: Sharppy: Fueling the python cult. *5th Sympos-
657 ium on Advances in Modeling and Analysis Using Python*, Phoenix, AZ, Amer. Meteor. Soc.,
658 [Available online at <https://ams.confex.com/ams/95Annual/webprogram/Paper270233.html>.].
- 659 Jiménez, P. A., J. Dudhia, J. F. González-Rouco, J. Navarro, J. P. Montávez, and E. García-
660 Bustamante, 2012: A revised scheme for the wrf surface layer formulation. *Mon. Wea. Rev.*,
661 **140** (3), 898–918.
- 662 Klemp, J. B., and R. Rotunno, 1983: A study of the tornadic region within a supercell thunder-
663 storm. *J. Atmos. Sci.*, **40** (2), 359–377.
- 664 Klemp, J. B., and R. B. Wilhelmson, 1978: The simulation of three-dimensional convective storm
665 dynamics. *J. Atmos. Sci.*, **35** (6), 1070–1096.

- 666 Mansell, E. R., 2010: On sedimentation and advection in multimoment bulk microphysics. *J.
667 Atmos. Sci.*, **67** (9), 3084–3094.
- 668 Mansell, E. R., C. L. Ziegler, and E. C. Bruning, 2010: Simulated electrification of a small thun-
669 derstorm with two-moment bulk microphysics. *J. Atmos. Sci.*, **67** (1), 171–194.
- 670 Markowski, P., C. Hannon, J. Frame, E. Lancaster, A. Pietrycha, R. Edwards, and R. L. Thompson,
671 2003: Characteristics of vertical wind profiles near supercells obtained from the rapid update
672 cycle. *Wea. Forecasting*, **18** (6), 1262–1272.
- 673 Markowski, P., and Y. Richardson, 2010: *Mesoscale Meteorology in Midlatitudes*. Wiley-
674 Blackwell, 372 pp.
- 675 Markowski, P., Y. Richardson, and G. Bryan, 2014: The origins of vortex sheets in a simulated
676 supercell thunderstorm. *Mon. Wea. Rev.*, **142** (11), 3944–3954.
- 677 Markowski, P., Y. Richardson, E. Rasmussen, J. Straka, R. Davies-Jones, and R. J. Trapp, 2008:
678 Vortex lines within low-level mesocyclones obtained from pseudo-dual-doppler radar observa-
679 tions. *Mon. Wea. Rev.*, **136** (9), 3513–3535.
- 680 Markowski, P., and Coauthors, 2012a: The pretornadic phase of the goshen county, wyoming,
681 supercell of 5 june 2009 intercepted by vortex2. part i: Evolution of kinematic and surface
682 thermodynamic fields. *Mon. Wea. Rev.*, **140** (9), 2887–2915.
- 683 Markowski, P., and Coauthors, 2012b: The pretornadic phase of the goshen county, wyoming,
684 supercell of 5 june 2009 intercepted by vortex2. part ii: Intensification of low-level rotation.
685 *Mon. Wea. Rev.*, **140** (9), 2916–2938.
- 686 Markowski, P. M., 2002: Hook echoes and rear-flank downdrafts: A review. *Mon. Wea. Rev.*,
687 **130** (4), 852–876.

- 688 Markowski, P. M., 2016: An idealized numerical simulation investigation of the effects of surface
689 drag on the development of near-surface vorticity in supercell thunderstorms. *J. Atmos. Sci.*,
690 submitted.
- 691 Markowski, P. M., and G. H. Bryan, 2016: Les of laminar flow in the pbl: A potential problem for
692 convective storm simulations. *Mon. Wea. Rev.*, **144** (5), 1841–1850.
- 693 Markowski, P. M., Y. Richardson, M. Majcen, J. Marquis, and J. Wurman, 2011: Characteristics of
694 the wind field in three nontornadic low-level mesocyclones observed by the doppler on wheels
695 radars. *Electronic J. Severe Storms Meteor.*, **6** (3).
- 696 Markowski, P. M., and Y. P. Richardson, 2014: The influence of environmental low-level shear
697 and cold pools on tornadogenesis: Insights from idealized simulations. *J. Atmos. Sci.*, **71** (1),
698 243–275.
- 699 Marquis, J., Y. Richardson, P. Markowski, D. Dowell, and J. Wurman, 2012: Tornado maintenance
700 investigated with high-resolution dual-doppler and enkf analysis. *Mon. Wea. Rev.*, **140** (1), 3–27.
- 701 Marquis, J., Y. Richardson, P. Markowski, D. Dowell, J. Wurman, K. Kosiba, P. Robinson, and
702 G. Romine, 2014: An investigation of the goshen county, wyoming, tornadic supercell of 5
703 june 2009 using enkf assimilation of mobile mesonet and radar observations collected during
704 vortex2. part i: Experiment design and verification of the enkf analyses. *Mon. Wea. Rev.*, **142** (2),
705 530–554.
- 706 Naylor, J., and M. S. Gilmore, 2012: Convective initiation in an idealized cloud model using an
707 updraft nudging technique. *Mon. Wea. Rev.*, **140** (11), 3699–3705.
- 708 Nowotarski, C., 2015: Low-level shear in the near-storm environment of simulated supercells
709 and impacts of shear orientation on outflow characteristics. *16th Conf. on Mesoscale Processes*,

- 710 Boston, MA, Amer. Meteor. Soc., [Available online at <https://ams.confex.com/ams/16Meso/webprogram/Paper274760.html>.].
- 711
- 712 Nowotarski, C. J., P. M. Markowski, Y. P. Richardson, and G. H. Bryan, 2015: Supercell low-level
713 mesocyclones in simulations with a sheared convective boundary layer. *Mon. Wea. Rev.*, **143** (1),
714 272–297.
- 715 Okubo, A., 1970: Horizontal dispersion of floatable particles in the vicinity of velocity singulari-
716 ties such as convergences. *Deep-Sea Res.*, **17** (3), 445–454.
- 717 Parker, M. D., 2012: Impacts of lapse rates on low-level rotation in idealized storms. *J. Atmos.*
718 *Sci.*, **69** (2), 538–559.
- 719 Parker, M. D., 2014: Composite vortex2 supercell environments from near-storm soundings. *Mon.*
720 *Wea. Rev.*, **142** (2), 508–529.
- 721 Parker, M. D., and J. M. Dahl, 2015: Production of near-surface vertical vorticity by idealized
722 downdrafts. *Mon. Wea. Rev.*, **143** (7), 2795–2816.
- 723 Rasmussen, E. N., 2003: Refined supercell and tornado forecast parameters. *Wea. Forecasting*,
724 **18** (3), 530–535.
- 725 Rasmussen, E. N., and D. O. Blanchard, 1998: A baseline climatology of sounding-derived super-
726 cell and tornado forecast parameters. *Wea. Forecasting*, **13** (4), 1148–1164.
- 727 Rasmussen, E. N., and J. M. Straka, 2007: Evolution of low-level angular momentum in the 2 june
728 1995 dimmitt, texas, tornado cyclone. *J. Atmos. Sci.*, **64** (4), 1365–1378.
- 729 Rasmussen, E. N., J. M. Straka, R. Davies-Jones, C. A. Doswell III, F. H. Carr, M. D. Eilts, and
730 D. R. MacGorman, 1994: Verification of the origins of rotation in tornadoes experiment: Vortex.
731 *Bull. Amer. Meteor. Soc.*, **75** (6), 995–1006.

- 732 Roberts, B., M. Xue, A. D. Schenkman, and D. T. Dawson, 2016: The role of surface
733 drag in tornadogenesis within an idealized supercell simulation. *J. Atmos. Sci.*, doi:10.1175/
734 JAS-D-15-0188.1, in press.
- 735 Rotunno, R., 2013: The fluid dynamics of tornadoes. *Annu. Rev. Fluid Mech.*, **45** (1), 59–84.
- 736 Rotunno, R., and J. Klemp, 1985: On the rotation and propagation of simulated supercell thunder-
737 storms. *J. Atmos. Sci.*, **42** (3), 271–292.
- 738 Schenkman, A. D., M. Xue, and M. Hu, 2014: Tornadogenesis in a high-resolution simulation of
739 the 8 may 2003 oklahoma city supercell. *J. Atmos. Sci.*, **71** (1), 130–154.
- 740 Shu, C.-W., 2003: High-order finite difference and finite volume weno schemes and discontinuous
741 galerkin methods for cfd. *Int. J. Comput. Fluid Dyn.*, **17** (2), 107–118.
- 742 Snyder, C., and F. Zhang, 2003: Assimilation of simulated doppler radar observations with an
743 ensemble kalman filter. *Mon. Wea. Rev.*, **131** (8), 1663–1677.
- 744 Straka, J. M., E. N. Rasmussen, R. P. Davies-Jones, and P. M. Markowski, 2007: An observational
745 and idealized numerical examination of low-level counter-rotating vortices in the rear flank of
746 supercells. *Electronic J. Severe Storms Meteor.*, **2** (8).
- 747 Thompson, R. L., R. Edwards, J. A. Hart, K. L. Elmore, and P. Markowski, 2003: Close proximity
748 soundings within supercell environments obtained from the rapid update cycle. *Wea. Forecast-
749 ing*, **18** (6), 1243–1261.
- 750 Thompson, R. L., C. M. Mead, and R. Edwards, 2007: Effective storm-relative helicity and bulk
751 shear in supercell thunderstorm environments. *Wea. Forecasting*, **22** (1), 102–115.

- 752 Thompson, R. L., B. T. Smith, J. S. Grams, A. R. Dean, and C. Broyles, 2012: Convective modes
753 for significant severe thunderstorms in the contiguous united states. part ii: Supercell and qlcs
754 tornado environments. **27** (5), 1136–1154.
- 755 Trapp, R., 1999: Observations of nontornadic low-level mesocyclones and attendant tornadogen-
756 esis failure during vortex. *Mon. Wea. Rev.*, **127** (7), 1693–1705.
- 757 Trapp, R. J., and R. Davies-Jones, 1997: Tornadogenesis with and without a dynamic pipe effect.
758 *J. Atmos. Sci.*, **54** (1), 113–133.
- 759 Trapp, R. J., G. J. Stumpf, and K. L. Manross, 2005: A reassessment of the percentage of tornadic
760 mesocyclones. *Wea. Forecasting*, **20** (4), 680–687.
- 761 Wakimoto, R. M., and H. Cai, 2000: Analysis of a nontornadic storm during vortex 95. *Mon. Wea.*
762 *Rev.*, **128** (3), 565–592.
- 763 Wakimoto, R. M., H. Cai, and H. V. Murphey, 2004: The superior, nebraska, supercell during
764 bamex. *Bull. Amer. Meteor. Soc.*, **85** (8), 1095–1106.
- 765 Weiss, J., 1991: The dynamics of enstrophy transfer in two-dimensional hydrodynamics. *Physica*
766 *D*, **48** (2-3), 273–294.
- 767 Wicker, L. J., and W. C. Skamarock, 2002: Time-splitting methods for elastic models using for-
768 ward time schemes. *Mon. Wea. Rev.*, **130** (8), 2088–2097.
- 769 Wicker, L. J., and R. B. Wilhelmson, 1995: Simulation and analysis of tornado development and
770 decay within a three-dimensional supercell thunderstorm. *J. Atmos. Sci.*, **52** (15), 2675–2703.
- 771 Wilhelmson, R. B., and C.-S. Chen, 1982: A simulation of the development of successive cells
772 along a cold outflow boundary. *J. Atmos. Sci.*, **39** (7), 1466–1483.

- 773 Wurman, J., D. Dowell, Y. Richardson, P. Markowski, E. Rasmussen, D. Burgess, L. Wicker, and
- 774 H. B. Bluestein, 2012: The second verification of the origins of rotation in tornadoes experi-
- 775 ment: Vortex2. *Bull. Amer. Meteor. Soc.*, **93** (8), 1147–1170.
- 776 Ziegler, C. L., 1985: Retrieval of thermal and microphysical variables in observed convective
- 777 storms. part 1: Model development and preliminary testing. *J. Atmos. Sci.*, **42** (14), 1487–1509.

778 **LIST OF TABLES**

779 **Table 1.** Summary of common environmental forecasting parameters calculated from
780 the steady-state nontornadic and tornadic VORTEX2 near-inflow composite
781 soundings. The surface-based parcel is used for the convective available
782 potential energy (CAPE; $J\ kg^{-1}$), convective inhibition (CIN; $J\ kg^{-1}$), and the
783 lifted condensation level (LCL; m). The effective environmental bulk vertical
784 wind shear vector magnitude (kts) is simply referred to as effective shear
785 (Thompson et al. 2007). Storm-relative helicity (SRH; $m^2\ s^{-2}$) was calculated
786 using the Bunkers storm motion (Bunkers et al. 2000). The critical angle (deg)
787 is the angle between the 10 - 500 m wind shear vector and the 10 m wind
788 vector (Esterheld and Giuliano 2008), and the supercell composite parameter
789 (SCP; dimensionless) and significant tornado parameter (STP; dimensionless)
790 utilize the CIN constraint and the effective inflow layer described by Thompson
791 et al. (2007). All parameters were calculated using SHARPpy (Halbert et al.
792 2015).

39

793 **Table 2.** Summary of 0 - 500 m wind shear magnitude ($m\ s^{-1}$) and storm-relative helicity
794 (SRH; $m^2\ s^{-2}$) for the nontornadic and tornadic VORTEX2 composite
795 wind profiles. The parameters for the simulations with Coriolis applied to the
796 perturbation winds were computed at $t = 4$ hr in the small-domain simulation.
797 Parameters for the without Coriolis simulations were computed at $t = 2$ hr in a
798 separate small-domain simulation. The environmental bulk vertical wind shear
799 vector magnitude is simply referred to as shear, and SRH was calculated using
800 the Bunkers storm motion (Bunkers et al. 2000).

40

TABLE 1. Summary of common environmental forecasting parameters calculated from the steady-state
 nontornadic and tornadic VORTEX2 near-inflow composite soundings. The surface-based parcel is used for the convective available potential energy (CAPE; J kg^{-1}), convective inhibition (CIN; J kg^{-1}), and the lifted condensation level (LCL; m). The effective environmental bulk vertical wind shear vector magnitude (kts) is simply referred to as effective shear (Thompson et al. 2007). Storm-relative helicity (SRH; $\text{m}^2 \text{ s}^{-2}$) was calculated using the Bunkers storm motion (Bunkers et al. 2000). The critical angle (deg) is the angle between the 10 - 500 m wind shear vector and the 10 m wind vector (Esterheld and Giuliano 2008), and the supercell composite parameter (SCP; dimensionless) and significant tornado parameter (STP; dimensionless) utilize the CIN constraint and the effective inflow layer described by Thompson et al. (2007). All parameters were calculated using SHARPpy (Halbert et al. 2015).

	CAPE	CIN	LCL	effective shear	0 – 500 m SRH	0 – 1 km SRH	effective SRH	critical angle	SCP	STP
Nontornadic	2377	-43	1129	49	80	151	314	140	14.9	2.6
Tornadic	2755	-39	845	61	159	224	297	93	16.4	4.9

811 TABLE 2. Summary of 0 - 500 m wind shear magnitude (m s^{-1}) and storm-relative helicity (SRH; $\text{m}^2 \text{s}^{-2}$)
 812 for the nontornadic and tornadic VORTEX2 composite wind profiles. The parameters for the simulations with
 813 Coriolis applied to the perturbation winds were computed at $t = 4$ hr in the small-domain simulation. Parameters
 814 for the without Coriolis simulations were computed at $t = 2$ hr in a separate small-domain simulation. The
 815 environmental bulk vertical wind shear vector magnitude is simply referred to as shear, and SRH was calculated
 816 using the Bunkers storm motion (Bunkers et al. 2000).

	0 – 500 m shear	0 – 500 m SRH
Nontornadic		
Original	6.9	85.3
W/ Coriolis	6.7	80.2
W/o Coriolis	6.4	100.4
Tornadic		
Original	7.2	137.7
W/ Coriolis	8.3	158.6
W/o Coriolis	10.1	174.7

817 LIST OF FIGURES

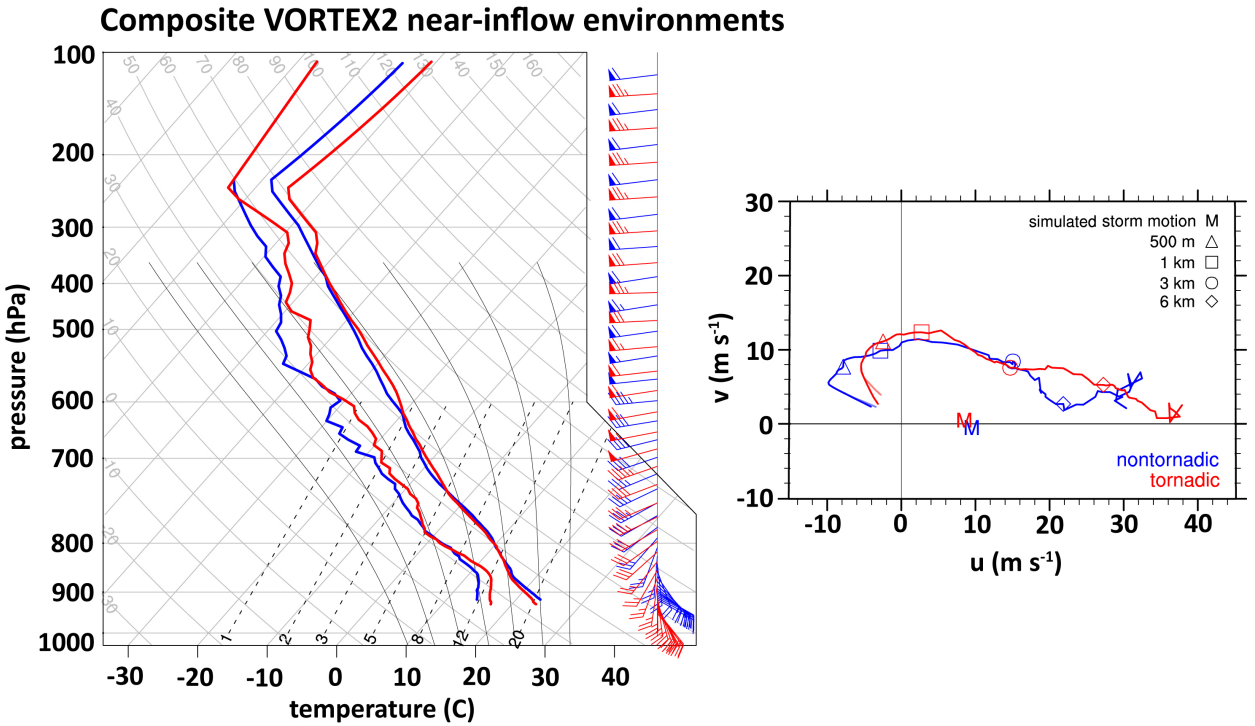
818	Fig. 1. (left) Skew T -log p diagram and (right) hodograph showing the steady-state, nontornadic 819 (blue) and tornadic (red) VORTEX2 near-inflow composite soundings. The original non- 820 tornadic and tornadic VORTEX near-inflow wind-profiles from Parker (2014) are superim- 821 posed on the hodograph (the subtle differences are confined to the lowest ~ 200 m). The 822 simulated storm motion is indicated on the hodograph by the "M". Markers on the hodo- 823 graph represent 500 m (triangle), 1 km (square), 3 km (circle), and 6 km (diamond) AGL. 824 The wind barbs on the skew T -log p are displayed in kt (1 kt = 50.5144 m s $^{-1}$).	44
825	Fig. 2. Horizontal cross sections of 500 m model-simulated reflectivity and 20 m s $^{-1}$ vertical ve- 826 locity at 3 km (black contour) at 5 min intervals from $t = 35 - 90$ min.	45
827	Fig. 3. As in Figure 2, except for the tornadic VORTEX2 simulation.	46
828	Fig. 4. Timeheight plot of the maximum vertical velocity (m s $^{-1}$) in a 50 km 2 box following the 829 mid-level mesocyclone for (left) the nontornadic VORTEX2 simulation and (right) the tor- 830 nadic VORTEX2 simulation.	47
831	Fig. 5. As in Figure 4, except for the maximum vertical vorticity (s $^{-1}$).	48
832	Fig. 6. Horizontal cross section from the tornadic VORTEX2 simulation at $t = 45$ min. (a) 500 833 m model-simulated reflectivity (\sim dBZ; shaded) and manually annotated boundaries. (b) 834 1 km vertical velocity (m s $^{-1}$; shaded), 10 dBZ reflectivity at 500 m (black contour). (c) 835 10 m density potential temperature perturbation (K; shaded), 10 dBZ reflectivity at 500 m 836 (black contour), 10 m Okubo-Weiss parameter greater than 0.01 s $^{-2}$ (filled cyan contour, if 837 present), 10 m storm-relative, horizontal wind vectors. (d) 10 m vertical vorticity (s $^{-1} \times$ 838 10 2 ; shaded), 10 dBZ reflectivity at 500 m (black contour), 10 m storm-relative, horizontal 839 vorticity vectors. For both (c) and (d) every fourth vector is plotted. The Okubo-Weiss 840 parameter is given by: $OW = \zeta^2 - D^2$, where the total deformation ($D = [D^2_{\text{stretching}} +$ 841 $D^2_{\text{shearing}}]^{1/2}$) of the flow is subtracted from the vertical vorticity (ζ) to highlight the 842 rotation of the fluid (Okubo 1970; Weiss 1991). Boundary annotations were determined 843 subjectively based on density potential temperature perturbations and the wind field. See 844 also an animated version of this figure for the tornadic VORTEX2 simulation from $t = 40 -$ 845 90 (100x normal speed) in the online supplemental material.	49
846	Fig. 7. As in Figure 6, except for the tornadic VORTEX2 simulation at $t = 55$ min.	50
847	Fig. 8. As in Figure 6, except for the tornadic VORTEX2 simulation at $t = 60$ min.	51
848	Fig. 9. Three-dimensional view of the low-level mesocyclone and tornado for the tornadic VOR- 849 TEX2 supercell. Shaded on the surface is the 500 m model-simulated base reflectivity 850 (\sim dBZ). Updraft and Okubo-Weiss isosurfaces of 20 m s $^{-1}$ and 0.01 s $^{-1}$ are shown light 851 gray and black, respectively. See also an animated version of this figure (40x normal speed) 852 in the online supplemental material.	52
853	Fig. 10. As in Figure 6, except for the tornadic VORTEX2 simulation at $t = 75$ min.	53
854	Fig. 11. As in Figure 6, except for the nontornadic VORTEX2 simulation at $t = 60$ min. See also an 855 animated version of this figure for the nontornadic VORTEX2 simulation from $t = 40 - 90$ 856 (100x normal speed) in the online supplemental material.	54
857	Fig. 12. As in Figure 6, except for the nontornadic VORTEX2 simulation at $t = 70$ min.	55

858	Fig. 13. As in Figure 6, except for the nontornadic VORTEX2 simulation at $t = 80$ min.	56
859	Fig. 14. Time composite plot showing the average spatial (top) 1 km vertical velocity field (m s^{-1}),	
860	(middle) 10 m vertical vorticity field (s^{-1}), and (bottom) 10 m density potential temperature	
861	deficit (K) for (left) the nontornadic supercell and (right) the tornadic supercell. The 10	
862	m s^{-1} vertical velocity contour (green) at 1 km and the averaged 10 dBZ model-simulated	
863	reflectivity at 500 m (black contour) are shown for reference.	57
864	Fig. 15. Three-dimensional view of trajectories that acquired large near-surface vertical vorticity be-	
865	tween the lowest 3 vertical grid points (10 - 50 m) in both the (left) the nontornadic supercell	
866	and (right) the tornadic supercell during the final 5 minutes of the trajectory integration pe-	
867	riod. Shaded on the surface is average 10 m density potential temperature perturbation (K)	
868	during the same time period. A higher vertical vorticity threshold was applied in the tornadic	
869	supercell solely for clarity purposes.	58
870	Fig. 16. Time series comparing the dynamic vertical perturbation pressure gradient acceleration	
871	(VPPGA; m s^{-2}) and circulation ($\text{m}^2 \text{s}^{-1}$) for both the nontornadic (blue) and tornadic (red)	
872	supercells in a $50 \times 50 \text{ km}^2$ box following the supercell's mesocyclone. (top) The maximum	
873	acceleration value in both the 0 - 1 (left) and 0 - 3 km (right) layers. (bottom) The maximum	
874	circulation computed around a 1-km-radius horizontal ring centered at each grid point at	
875	the surface (dotted line) and 1 km (solid line) for the nontornadic and tornadic supercells.	
876	The bolded time periods represent the 15 minute time composite shown in Figure 14. A	
877	five-point smoother was used on each time series to account for jumps while tracking the	
878	supercell's mesocyclone.	59
879	Fig. 17. Horizontal cross sections of 0 - 1 km dynamic vertical perturbation pressure gradient ac-	
880	celeration (m s^{-2} ; shaded) and the 10 dBZ reflectivity at 500 m (black contour) from the	
881	nontornadic (top) and tornadic (bottom) VORTEX2 simulations.	60
882	Fig. 18. Horizontal cross sections of circulation ($\text{m}^2 \text{s}^{-1}$; shaded) computed around a 1-km-radius	
883	horizontal ring centered at each grid point at the surface and 1 km for the nontornadic super-	
884	cell and the 10 dBZ reflectivity contour (black). Also shown at 1 km is the 10 m s^{-1} vertical	
885	velocity contour (green) and the $\pm 2 \text{ hPa}$ dynamic nonlinear pressure perturbation (p'_{DNL})	
886	contour (red, if present). Vectors represent the perturbation horizontal velocity, plotting	
887	every fifth vector.	61
888	Fig. 19. As in Figure 18, except for the tornadic VORTEX2 simulation.	62
889	Fig. 20. Smoothed kernel density estimation violin plot of low-level mesocyclone parcel character-	
890	istics from the VORTEX2 simulations for the 500 parcels that acquired the highest vertical	
891	velocity, with vertical vorticity at least 0.01 s^{-1} , between 950 to 1050 m. From left to right:	
892	initial streamwise horizontal vorticity (s^{-1}), vertical velocity (m s^{-1}), and vertical vorticity	
893	(s^{-1}) for the nontornadic (blue) and tornadic (red) VORTEX2 simulations. The black line	
894	represents the median of the distribution.	63
895	Fig. 21. Horizontal cross sections of circulation ($\text{m}^2 \text{s}^{-1}$; shaded) at 1 km computed around a 1-	
896	km-radius horizontal ring centered at each grid point at the surface and 1 km for both the	
897	nontornadic (top) and tornadic (bottom) idealized simulations. Also shown is the 10 m	
898	s^{-1} vertical velocity contour (green) at 1 km. Vectors represent the perturbation horizontal	
899	velocity, plotted every fifth vector.	64

- Fig. 22.** Horizontal cross sections of 0 - 1 km dynamic vertical perturbation pressure gradient acceleration (m s^{-2} ; shaded) and the 10 m s^{-1} vertical velocity contour (green) at 1 km from the nontornadic (top) and tornadic (bottom) idealized simulations.

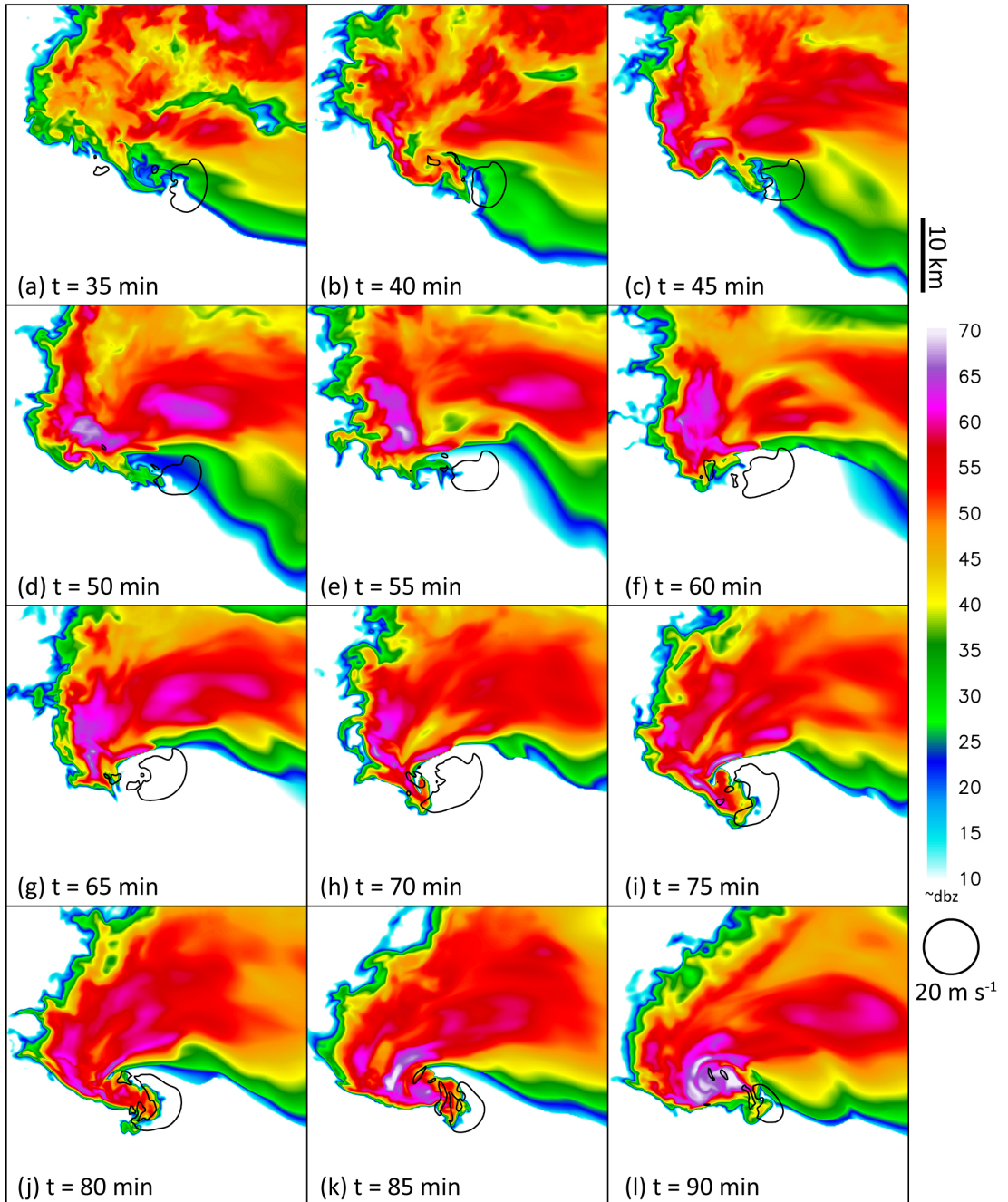
Fig. 23. Smoothed kernel density estimation violin plot of low-level mesocyclone parcel characteristics from the idealized simulations for all parcels that acquired vertical velocity of at least 10 m s^{-1} and vertical vorticity greater than 0.01 s^{-1} between 950 to 1050 m. From left to right: initial streamwise horizontal vorticity (s^{-1}), vertical velocity (m s^{-1}), vertical vorticity (s^{-1}), and vertical vorticity stretching ($\text{m}^2 \text{s}^{-2}$) for the nontornadic (blue) and tornadic (red) idealized simulations. The black line represents the median of the distribution, and the total number of low-level mesocyclone parcels beneath the legend.

Fig. 24. Conceptual schematic summarizing the key differences between the (a) nontornadic and (b) tornadic supercells. Schematic representations of the 0 - 500 m shear vector (\mathbf{S}_{0-500m}), low-level storm-relative winds, low-level updraft (dotted green contour), cyclonic circulation maximum (yellow arrow), and anticyclonic circulation maximum (blue arrow) presented accordingly. The shear vectors and low-level storm-relative are scaled proportionally in m s^{-1} . Hodograph diagrams showing the nontornadic (blue) and tornadic (red) VORTEX2 wind profiles from Figure 1 are also given.



917 FIG. 1. (left) Skew T -log p diagram and (right) hodograph showing the steady-state, nontornadic (blue) and
 918 tornadic (red) VORTEX2 near-inflow composite soundings. The original nontornadic and tornadic VORTEX
 919 near-inflow wind-profiles from Parker (2014) are superimposed on the hodograph (the subtle differences are
 920 confined to the lowest ~ 200 m). The simulated storm motion is indicated on the hodograph by the "M". Markers
 921 on the hodograph represent 500 m (triangle), 1 km (square), 3 km (circle), and 6 km (diamond) AGL. The wind
 922 barbs on the skew T -log p are displayed in kt (1 kt = 50.5144 m s $^{-1}$).

Nontornadic



923 FIG. 2. Horizontal cross sections of 500 m model-simulated reflectivity and 20 m s^{-1} vertical velocity at 3
924 km (black contour) at 5 min intervals from $t = 35 - 90 \text{ min}$.

Tornadic

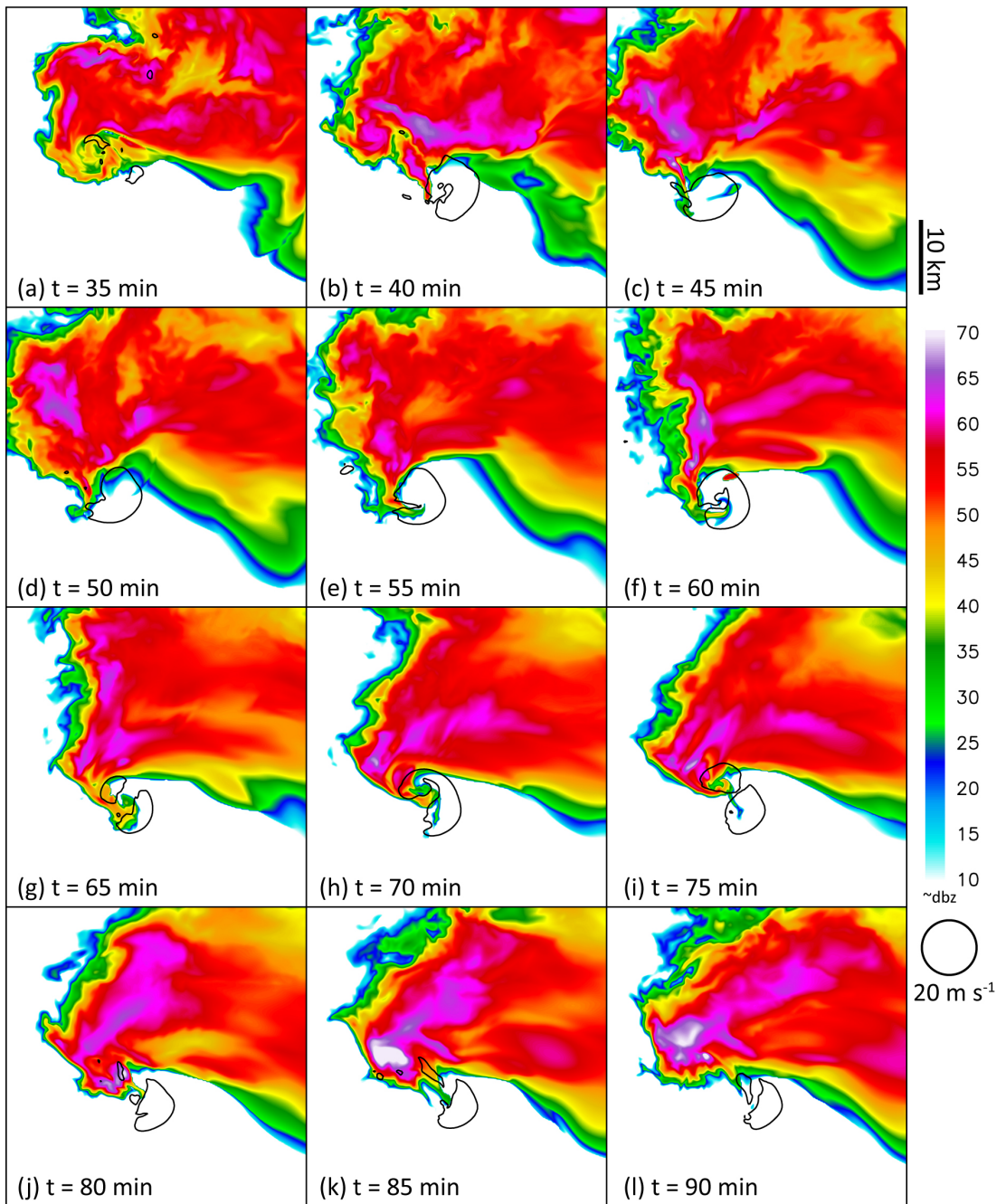
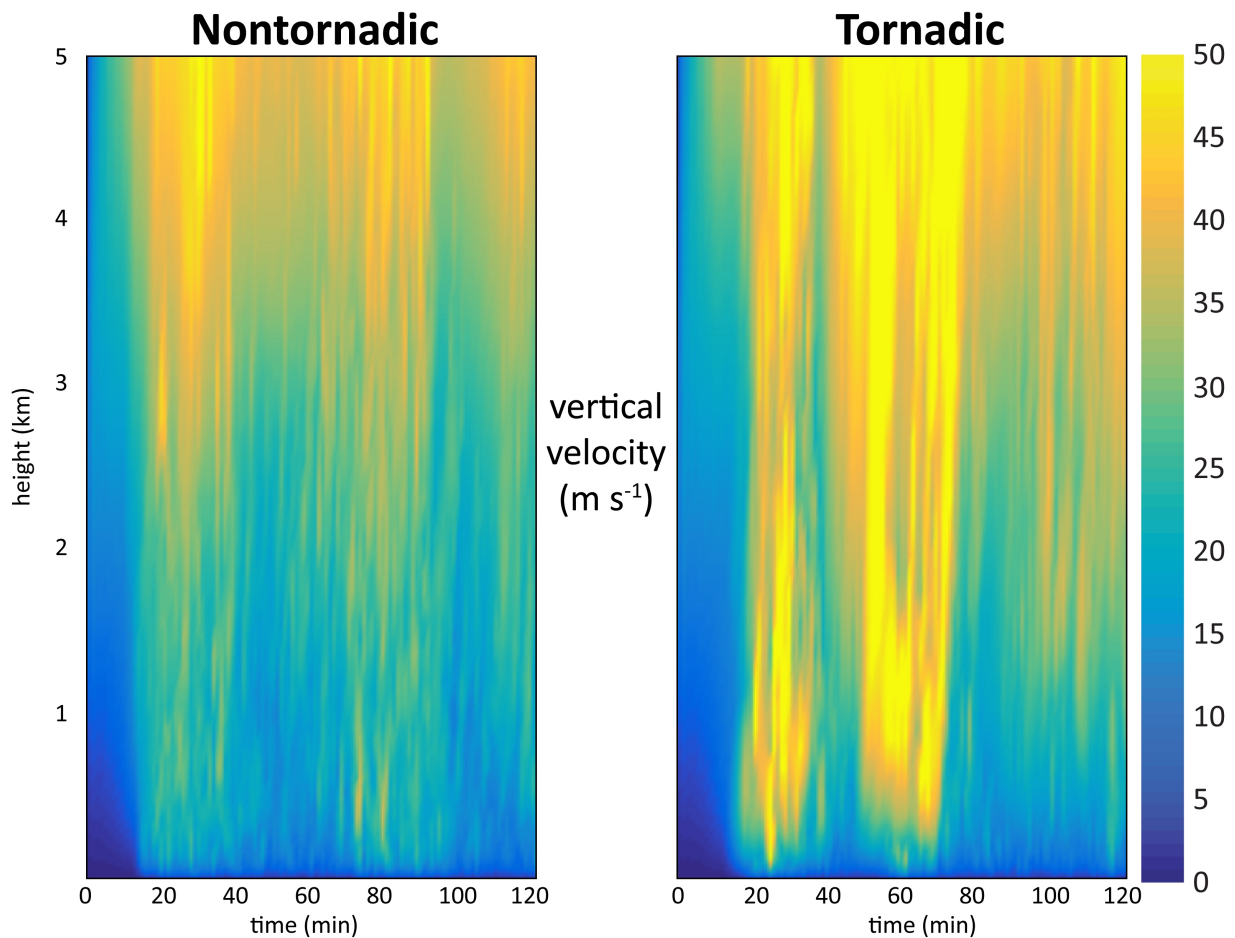


FIG. 3. As in Figure 2, except for the tornadic VORTEX2 simulation.



925 FIG. 4. Timeheight plot of the maximum vertical velocity (m s^{-1}) in a 50 km^2 box following the mid-level
 926 mesocyclone for (left) the nontornadic VORTEX2 simulation and (right) the tornadic VORTEX2 simulation.

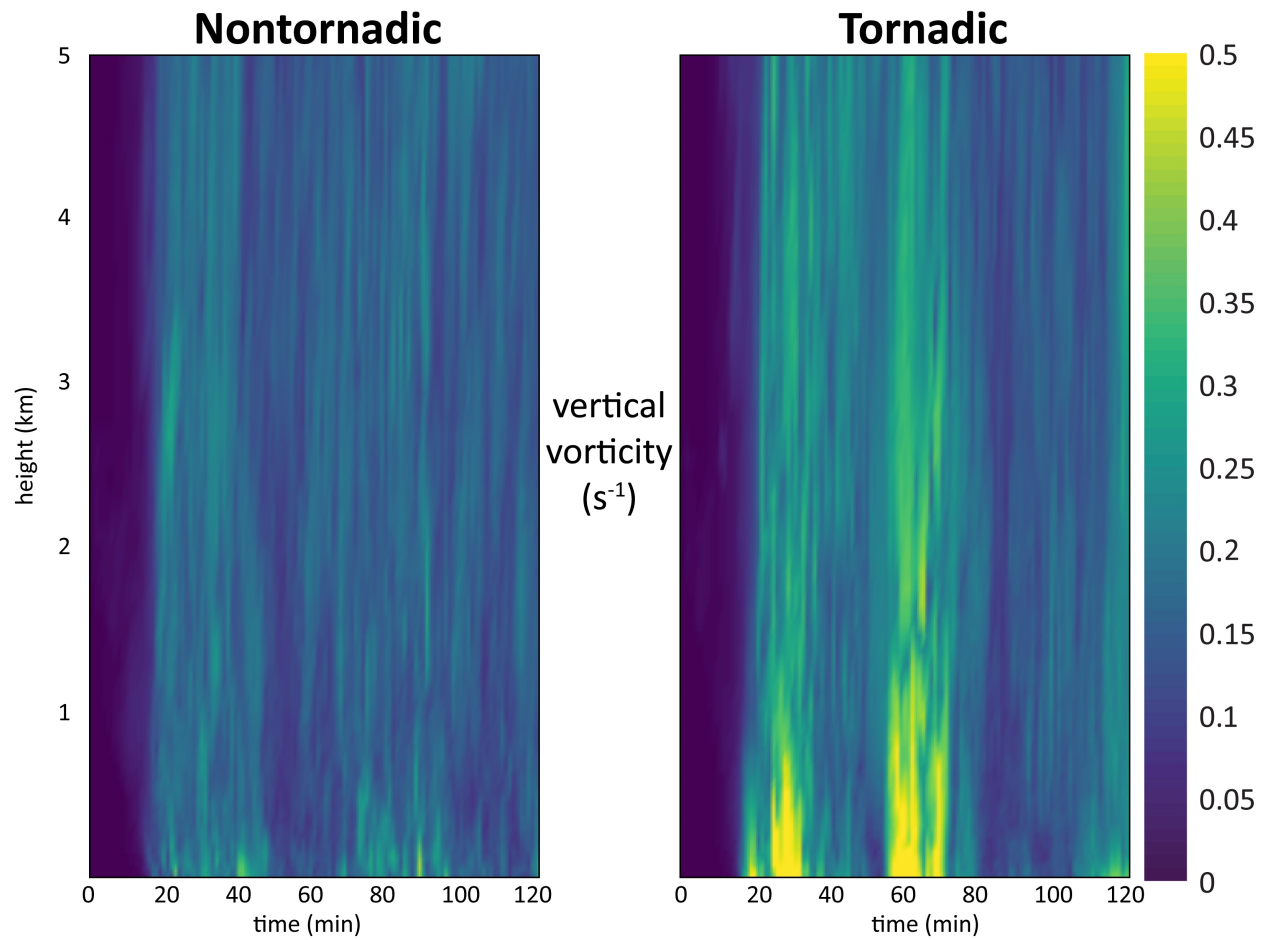


FIG. 5. As in Figure 4, except for the maximum vertical vorticity (s^{-1}).

Tornadic $t = 45$ min

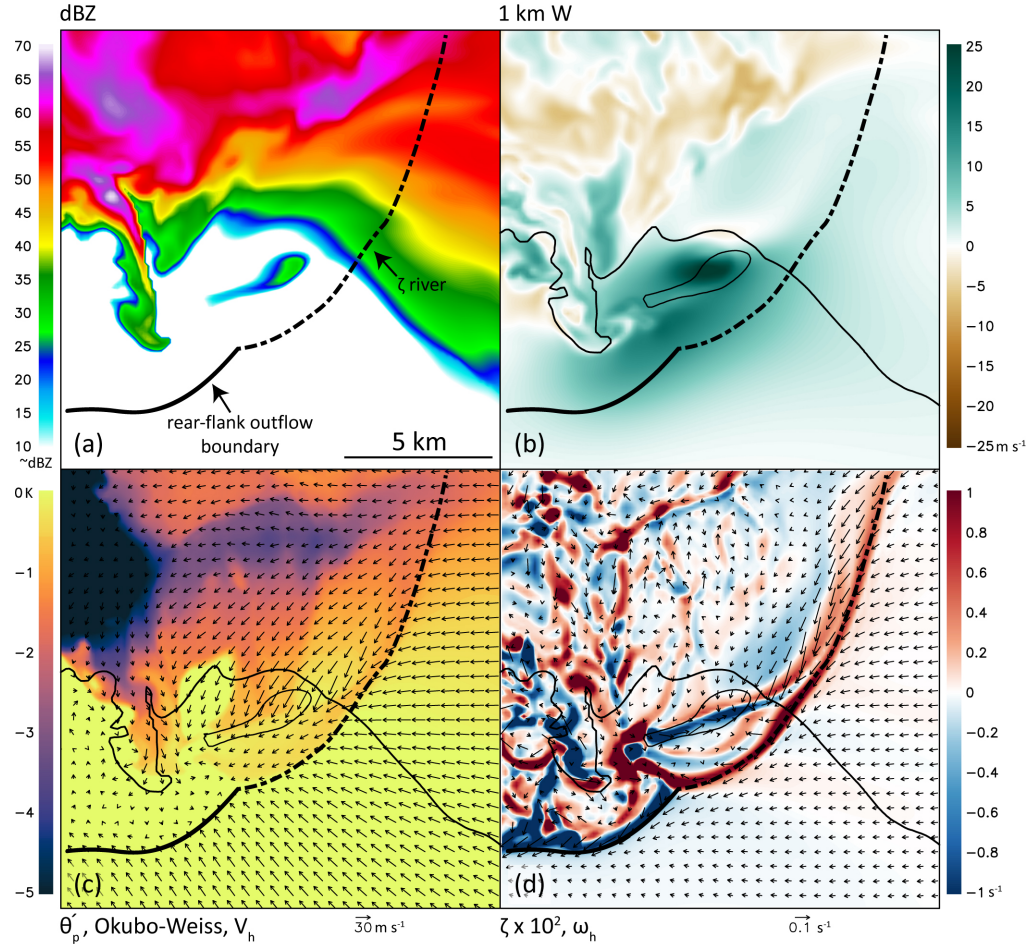


FIG. 6. Horizontal cross section from the tornadic VORTEX2 simulation at $t = 45$ min. (a) 500 m model-simulated reflectivity (\sim dBZ; shaded) and manually annotated boundaries. (b) 1 km vertical velocity ($m s^{-1}$; shaded), 10 dBZ reflectivity at 500 m (black contour). (c) 10 m density potential temperature perturbation (K; shaded), 10 dBZ reflectivity at 500 m (black contour), 10 m Okubo-Weiss parameter greater than $0.01 s^{-2}$ (filled cyan contour, if present), 10 m storm-relative, horizontal wind vectors. (d) 10 m vertical vorticity ($s^{-1} \times 10^2$; shaded), 10 dBZ reflectivity at 500 m (black contour), 10 m storm-relative, horizontal vorticity vectors. For both (c) and (d) every fourth vector is plotted. The Okubo-Weiss parameter is given by: $OW = \zeta^2 - D^2$, where the total deformation ($D = [D^2_{stretching} + D^2_{shearing}]^{1/2}$) of the flow is subtracted from the vertical vorticity (ζ) to highlight the rotation of the fluid (Okubo 1970; Weiss 1991). Boundary annotations were determined subjectively based on density potential temperature perturbations and the wind field. See also an animated version of this figure for the tornadic VORTEX2 simulation from $t = 40 - 90$ (100x normal speed) in the online supplemental material.

Tornadic $t = 55$ min

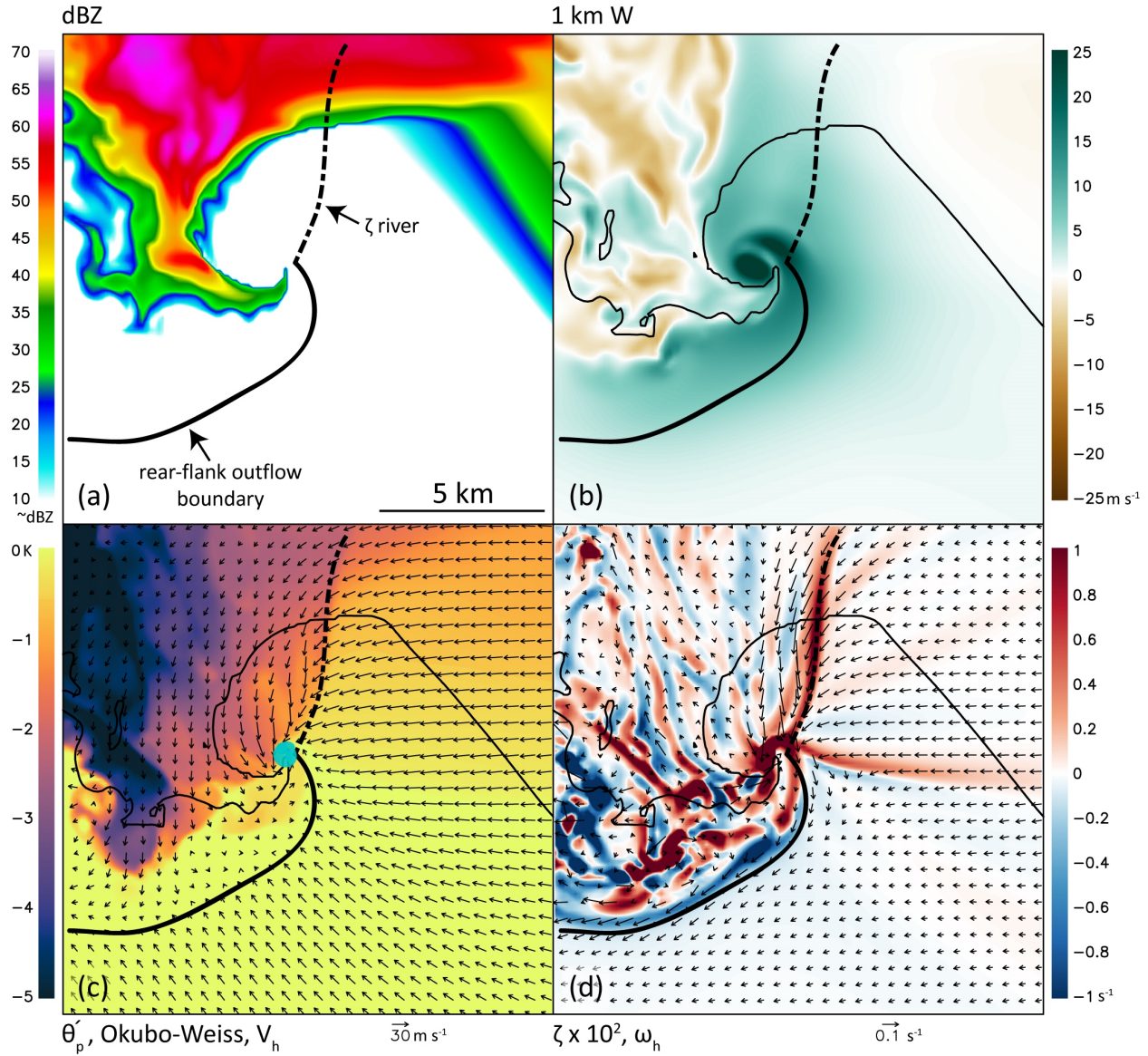


FIG. 7. As in Figure 6, except for the tornadic VORTEX2 simulation at $t = 55$ min.

Tornadic $t = 60$ min

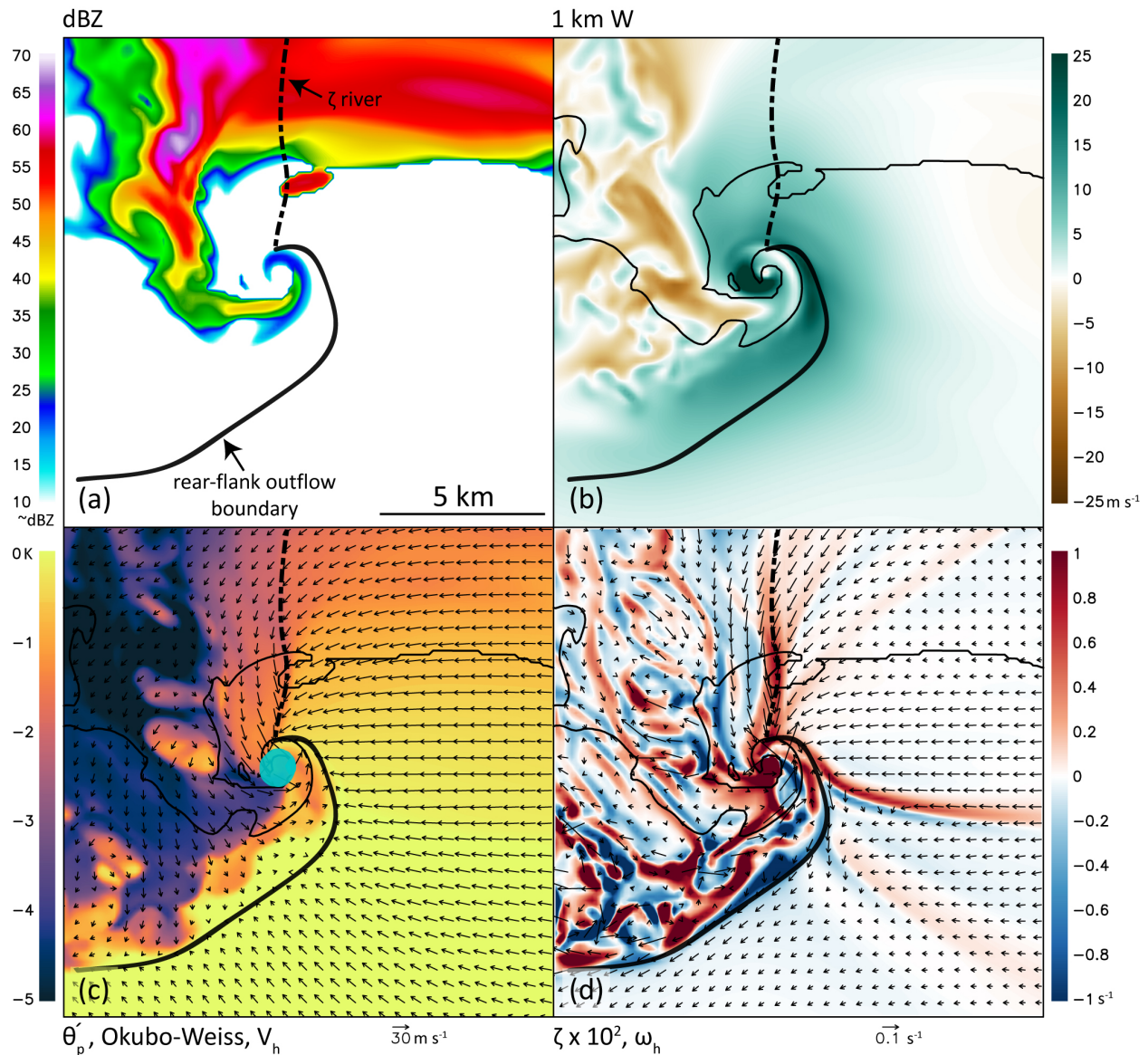
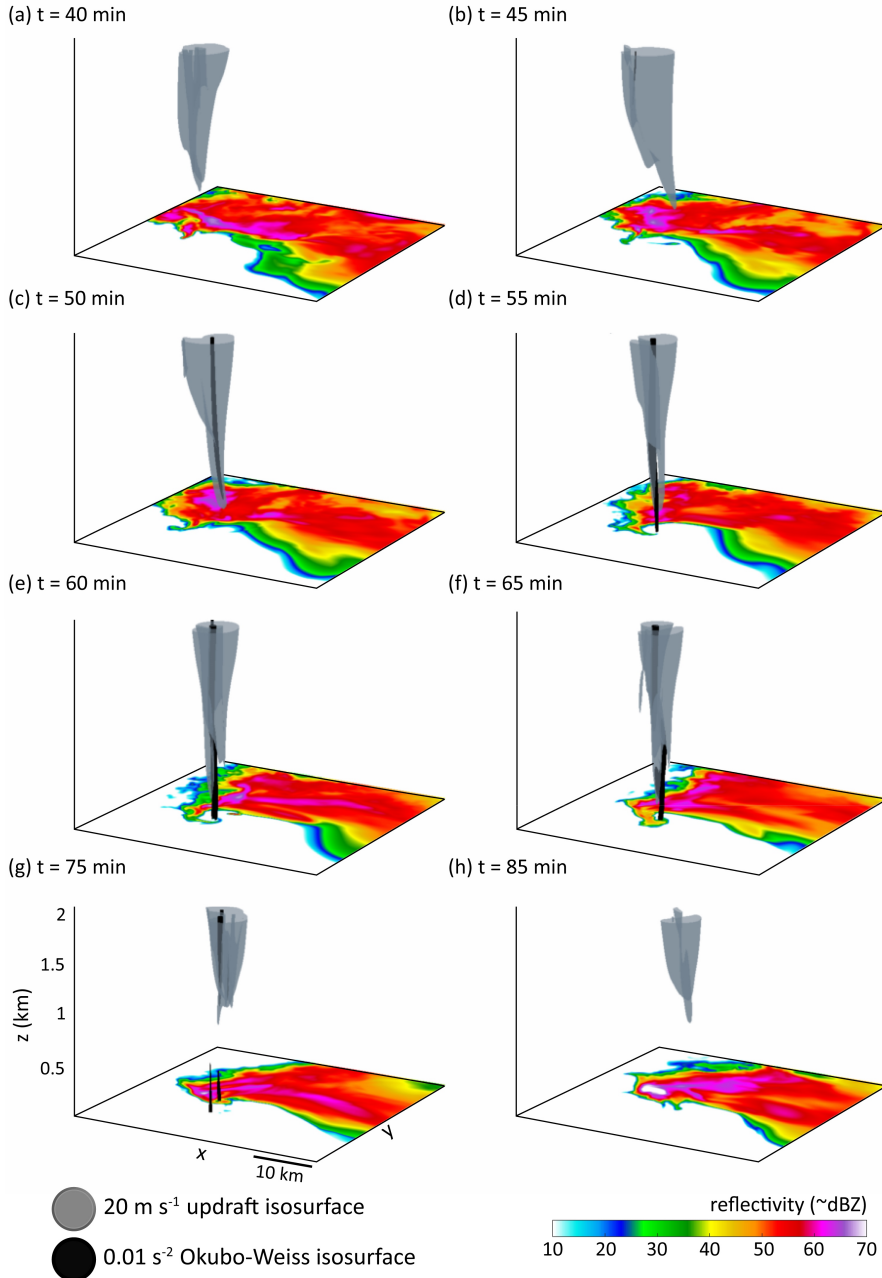


FIG. 8. As in Figure 6, except for the tornadic VORTEX2 simulation at $t = 60$ min.

Tornadic low-level mesocyclone



939 FIG. 9. Three-dimensional view of the low-level mesocyclone and tornado for the tornadic VORTEX2 super-
 940 cell. Shaded on the surface is the 500 m model-simulated base reflectivity ($\sim \text{dBZ}$). Updraft and Okubo-Weiss
 941 isosurfaces of 20 m s^{-1} and 0.01 s^{-2} are shown light gray and black, respectively. See also an animated version
 942 of this figure (40x normal speed) in the online supplemental material.

Tornadic $t = 75$ min

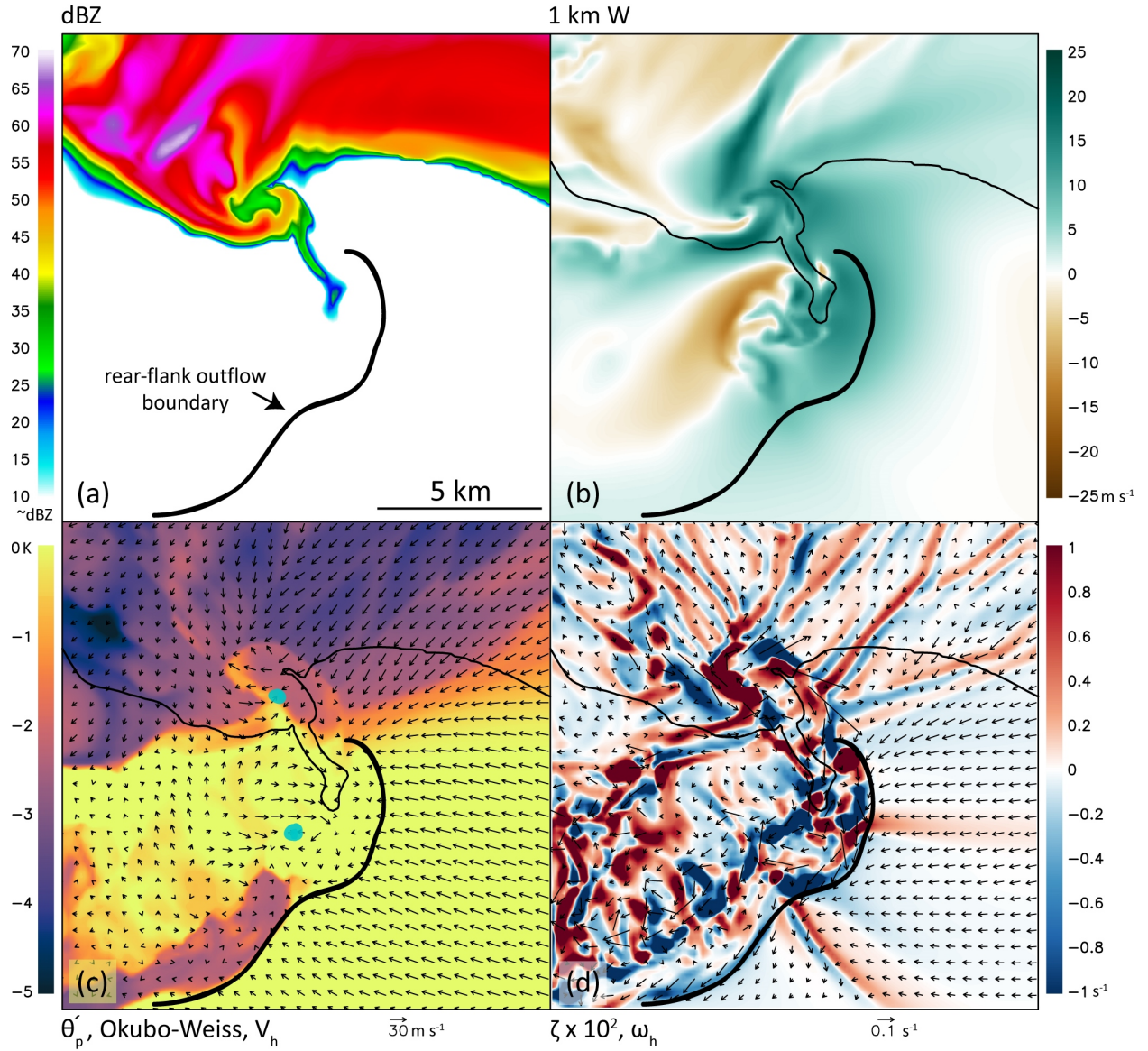


FIG. 10. As in Figure 6, except for the tornadic VORTEX2 simulation at $t = 75$ min.

Nontornadic $t = 60$ min

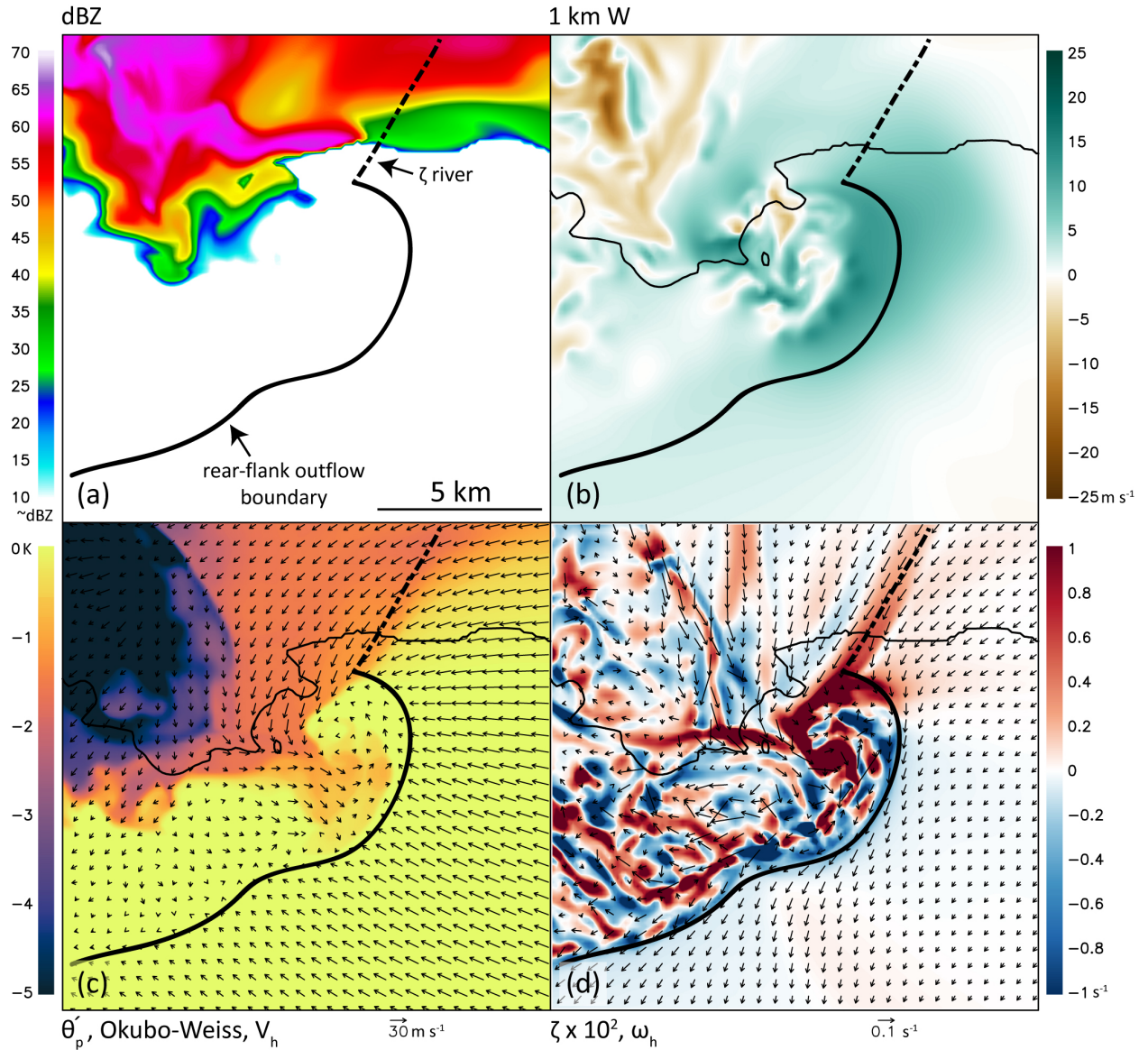


FIG. 11. As in Figure 6, except for the nontornadic VORTEX2 simulation at $t = 60$ min. See also an animated version of this figure for the nontornadic VORTEX2 simulation from $t = 40 - 90$ (100x normal speed) in the online supplemental material.

Nontornadic $t = 70$ min

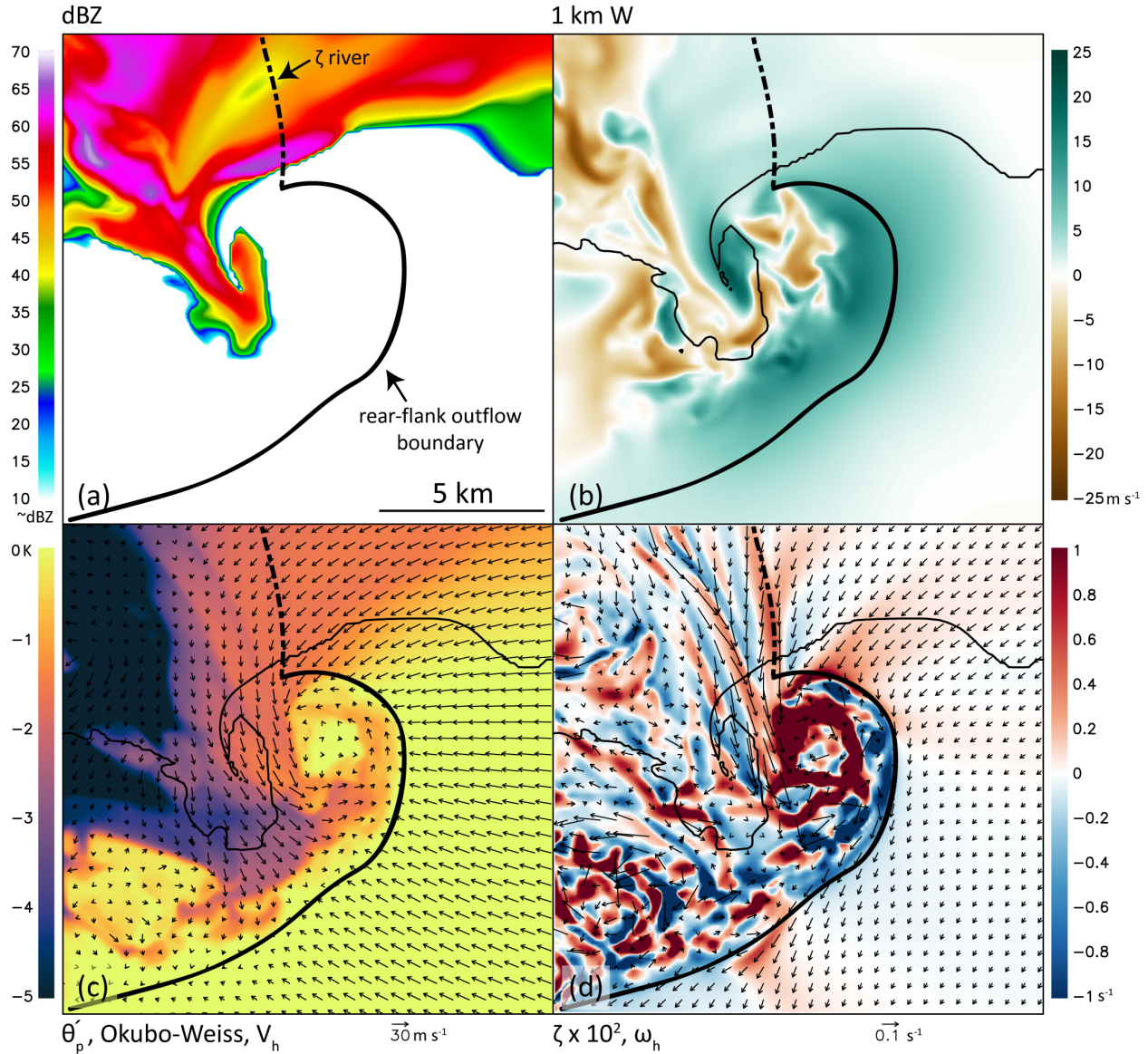


FIG. 12. As in Figure 6, except for the nontornadic VORTEX2 simulation at $t = 70$ min.

Nontornadic $t = 80$ min

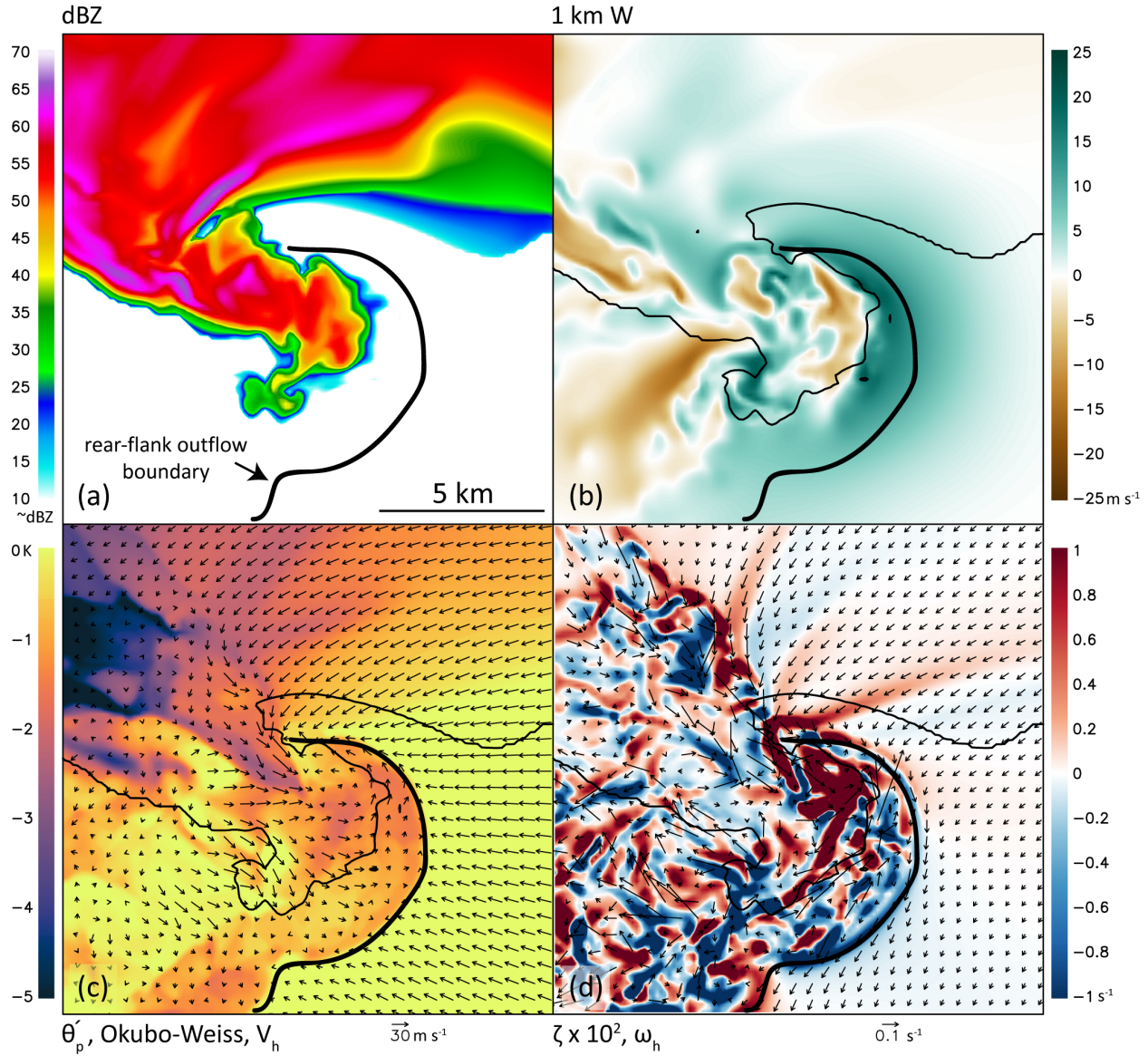


FIG. 13. As in Figure 6, except for the nontornadic VORTEX2 simulation at $t = 80$ min.

Time composite

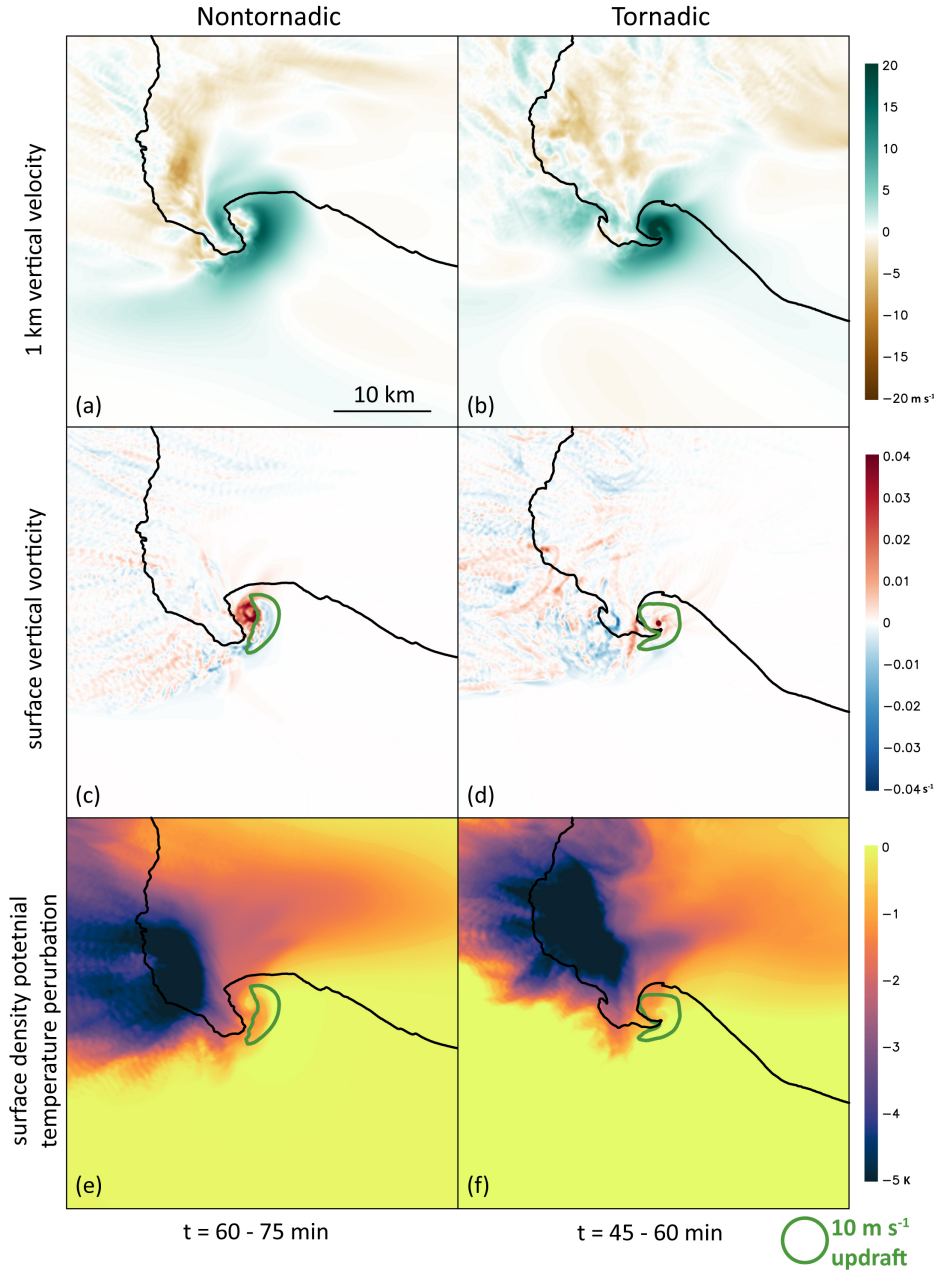


FIG. 14. Time composite plot showing the average spatial (top) 1 km vertical velocity field (m s^{-1}), (middle) 10 m s^{-1} vertical vorticity field (s^{-1}), and (bottom) 10 m s^{-1} density potential temperature deficit (K) for (left) the nontornadic supercell and (right) the tornadic supercell. The 10 m s^{-1} vertical velocity contour (green) at 1 km and the averaged 10 dBZ model-simulated reflectivity at 500 m (black contour) are shown for reference.

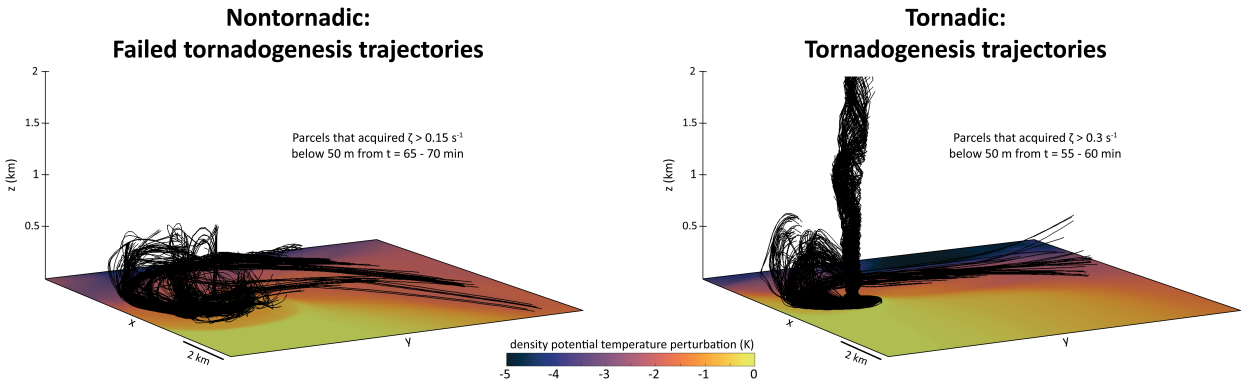


FIG. 15. Three-dimensional view of trajectories that acquired large near-surface vertical vorticity between the lowest 3 vertical grid points (10 - 50 m) in both the (left) the nontornadic supercell and (right) the tornadic supercell during the final 5 minutes of the trajectory integration period. Shaded on the surface is average 10 m density potential temperature perturbation (K) during the same time period. A higher vertical vorticity threshold was applied in the tornadic supercell solely for clarity purposes.

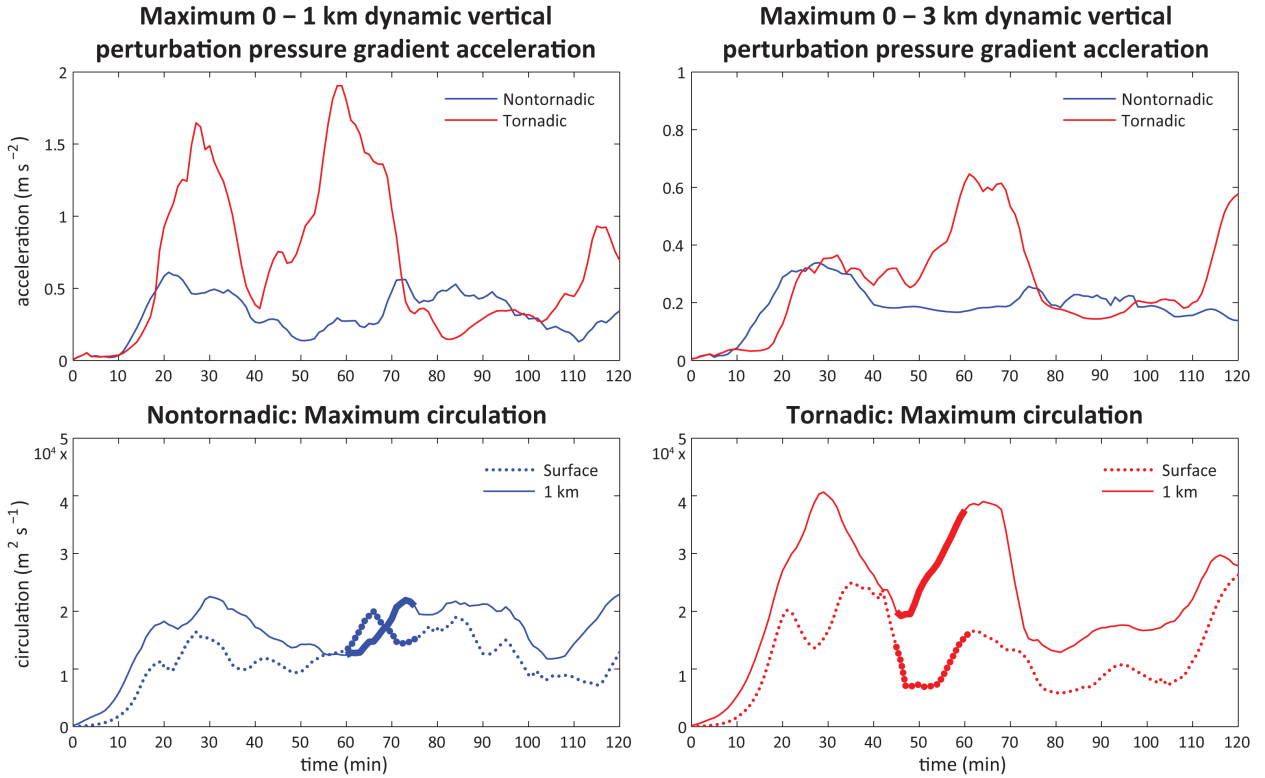


FIG. 16. Time series comparing the dynamic vertical perturbation pressure gradient acceleration (VPPGA; m s^{-2}) and circulation ($\text{m}^2 \text{s}^{-1}$) for both the nontornadic (blue) and tornadic (red) supercells in a $50 \times 50 \text{ km}^2$ box following the supercell's mesocyclone. (top) The maximum acceleration value in both the 0 - 1 (left) and 0 - 3 km (right) layers. (bottom) The maximum circulation computed around a 1-km-radius horizontal ring centered at each grid point at the surface (dotted line) and 1 km (solid line) for the nontornadic and tornadic supercells. The bolded time periods represent the 15 minute time composite shown in Figure 14. A five-point smoother was used on each time series to account for jumps while tracking the supercell's mesocyclone.

0 - 1 km dynamic vertical perturbation pressure gradient acceleration

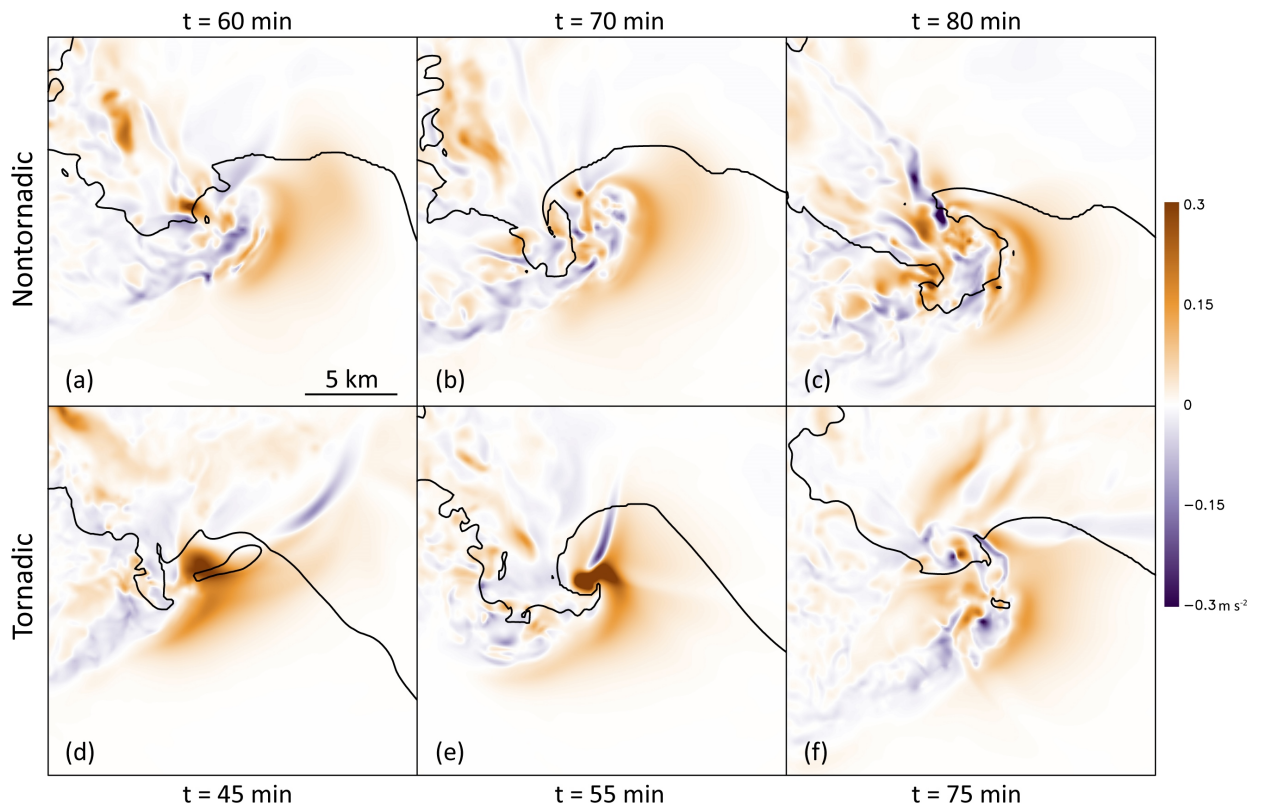


FIG. 17. Horizontal cross sections of 0 - 1 km dynamic vertical perturbation pressure gradient acceleration (m s^{-2} ; shaded) and the 10 dBZ reflectivity at 500 m (black contour) from the nontornadic (top) and tornadic (bottom) VORTEX2 simulations.

Circulation: Nontornadic

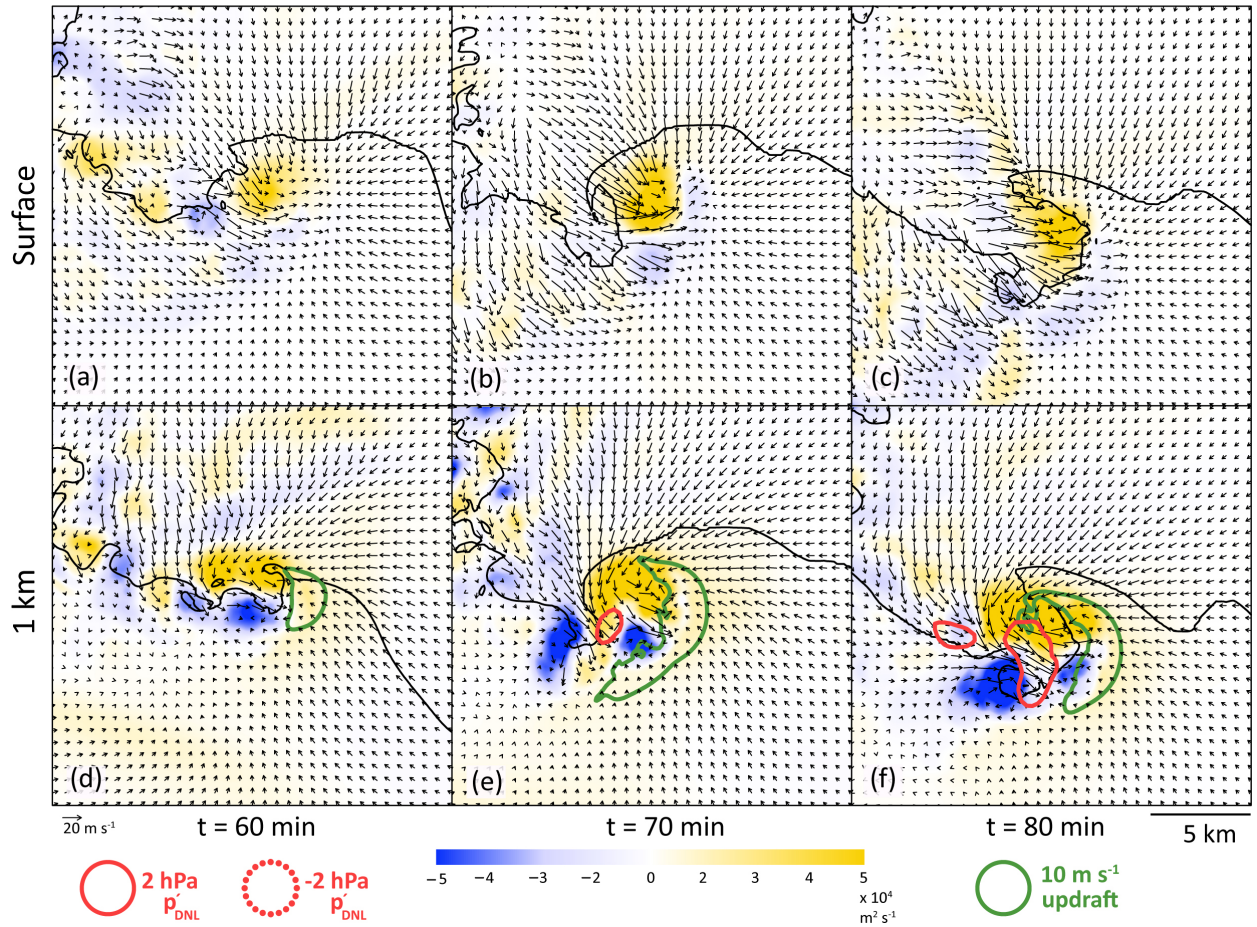


FIG. 18. Horizontal cross sections of circulation ($\text{m}^2 \text{ s}^{-1}$; shaded) computed around a 1-km-radius horizontal ring centered at each grid point at the surface and 1 km for the nontornadic supercell and the 10 dBZ reflectivity contour (black). Also shown at 1 km is the 10 m s^{-1} vertical velocity contour (green) and the $\pm 2 \text{ hPa}$ dynamic nonlinear pressure perturbation (p'_{DNL}) contour (red, if present). Vectors represent the perturbation horizontal velocity, plotting every fifth vector.

Circulation: Tornadic

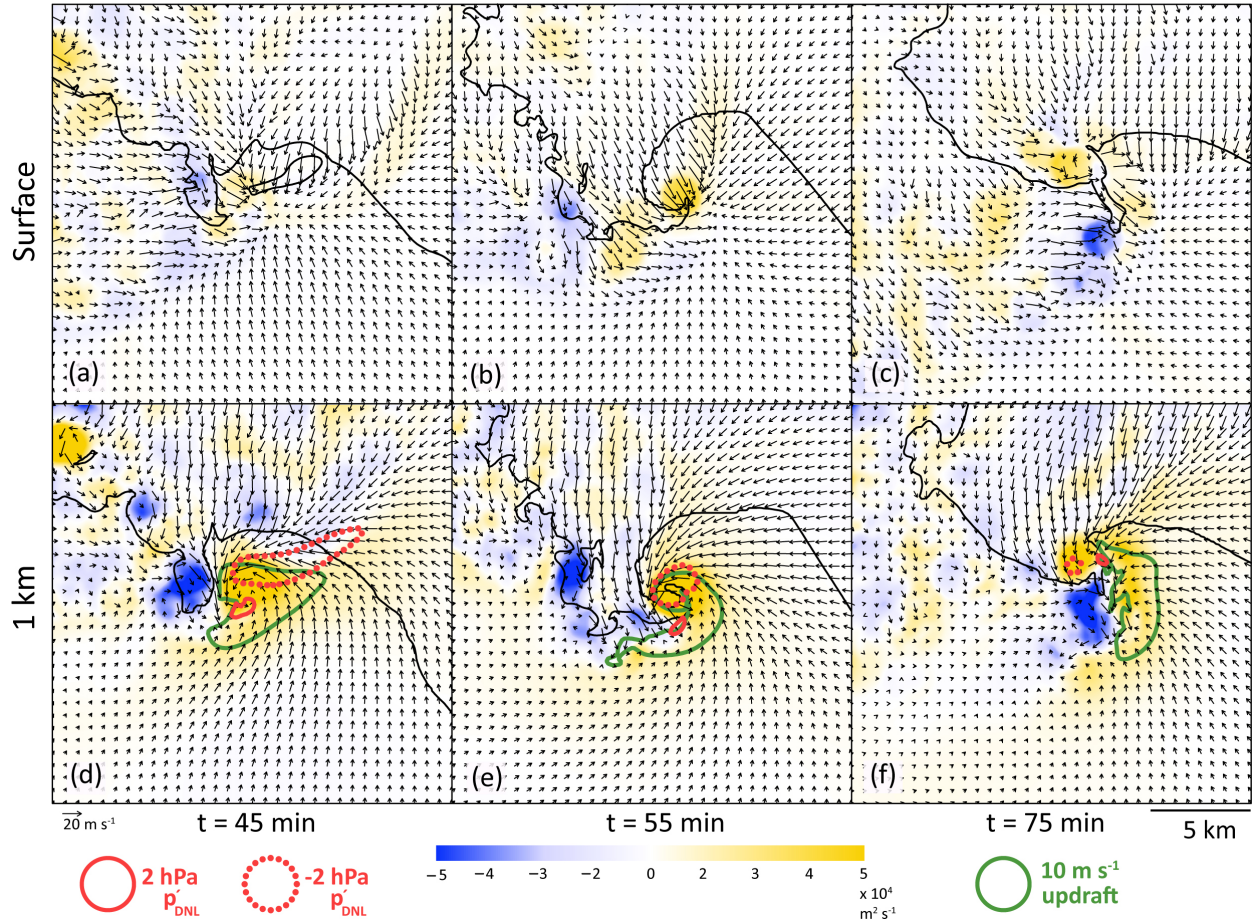


FIG. 19. As in Figure 18, except for the tornadic VORTEX2 simulation.

Low-level mesocyclone parcel characteristics

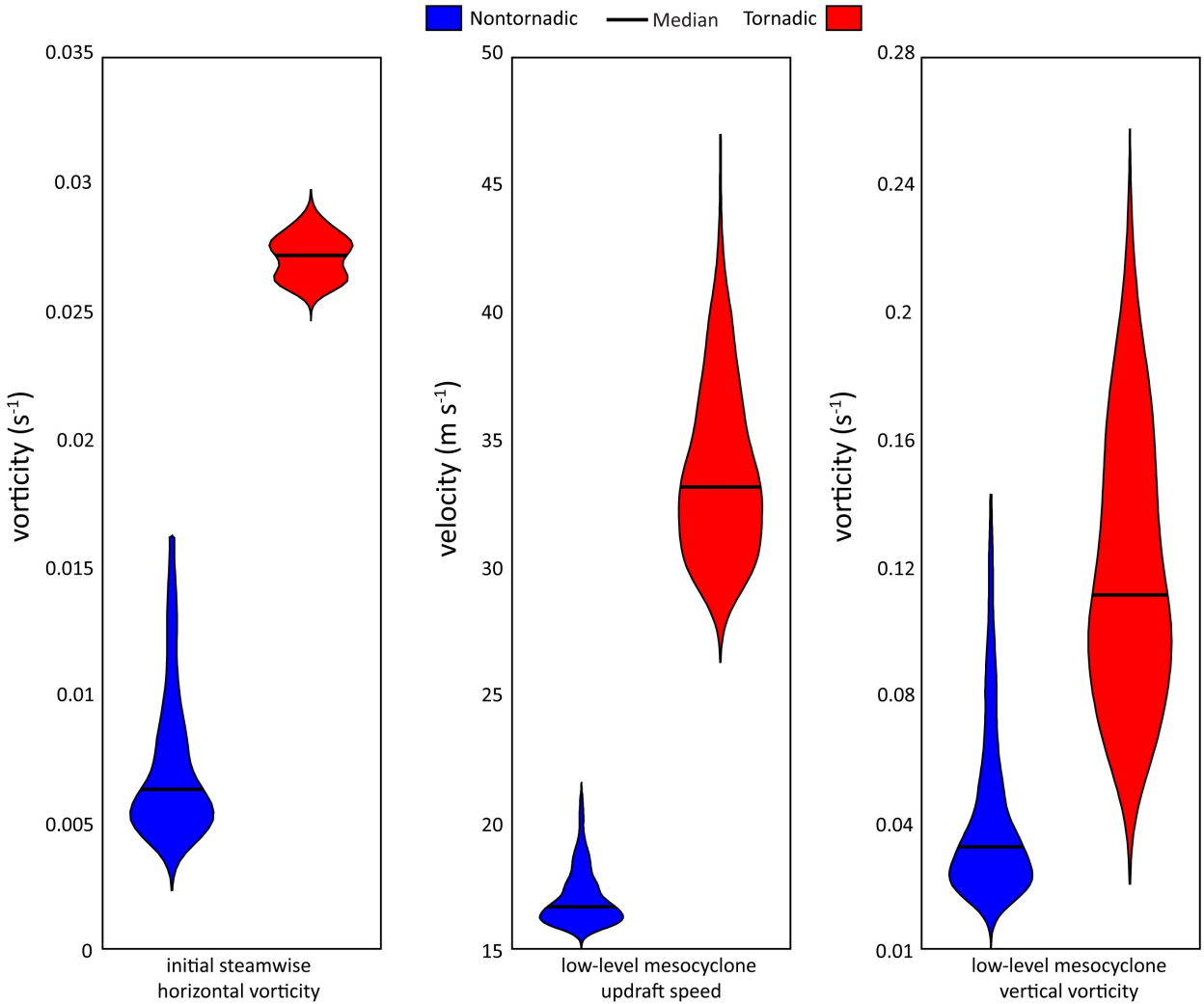


FIG. 20. Smoothed kernel density estimation violin plot of low-level mesocyclone parcel characteristics from the VORTEX2 simulations for the 500 parcels that acquired the highest vertical velocity, with vertical vorticity at least 0.01 s^{-1} , between 950 to 1050 m. From left to right: initial streamwise horizontal vorticity (s^{-1}), vertical velocity (m s^{-1}), and vertical vorticity (s^{-1}) for the nontornadic (blue) and tornadic (red) VORTEX2 simulations. The black line represents the median of the distribution.

Low-level circulation: Idealized simulations

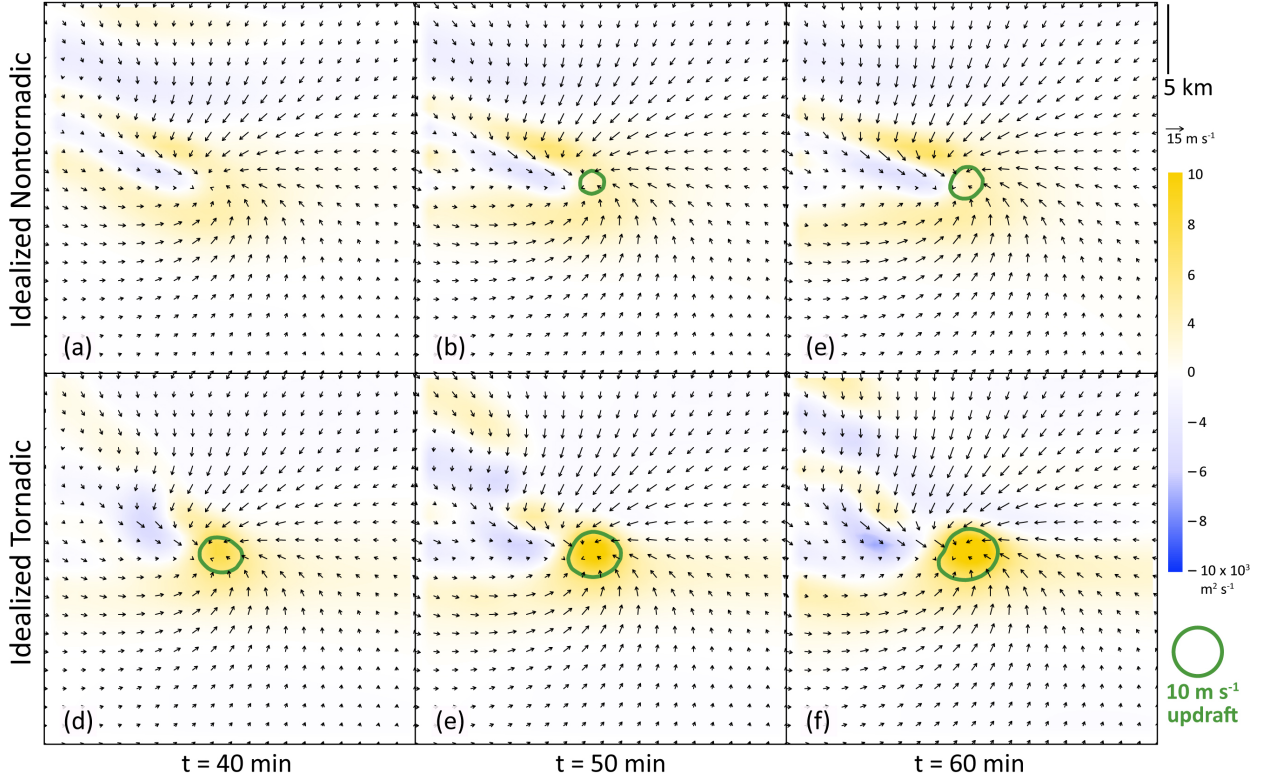
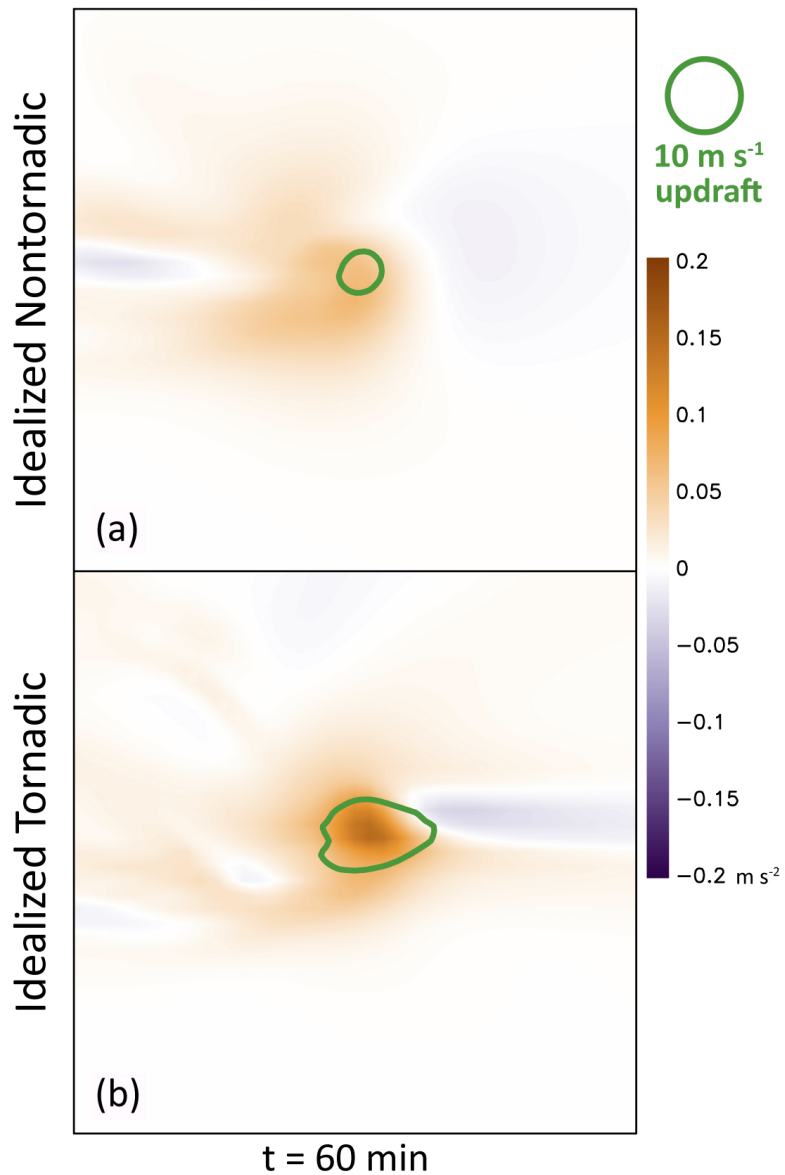


FIG. 21. Horizontal cross sections of circulation ($\text{m}^2 \text{ s}^{-1}$; shaded) at 1 km computed around a 1-km-radius horizontal ring centered at each grid point at the surface and 1 km for both the nontornadic (top) and tornadic (bottom) idealized simulations. Also shown is the 10 m s^{-1} vertical velocity contour (green) at 1 km. Vectors represent the perturbation horizontal velocity, plotted every fifth vector.

**0 - 1 km dynamic
vertical perturbation
pressure gradient acceleration**



979 FIG. 22. Horizontal cross sections of 0 - 1 km dynamic vertical perturbation pressure gradient acceleration (m
980 s^{-2} ; shaded) and the 10 m s^{-1} vertical velocity contour (green) at 1 km from the nontornadic (top) and tornadic
981 (bottom) idealized simulations.

Low-level mesocyclone parcel characteristics: Idealized simulations

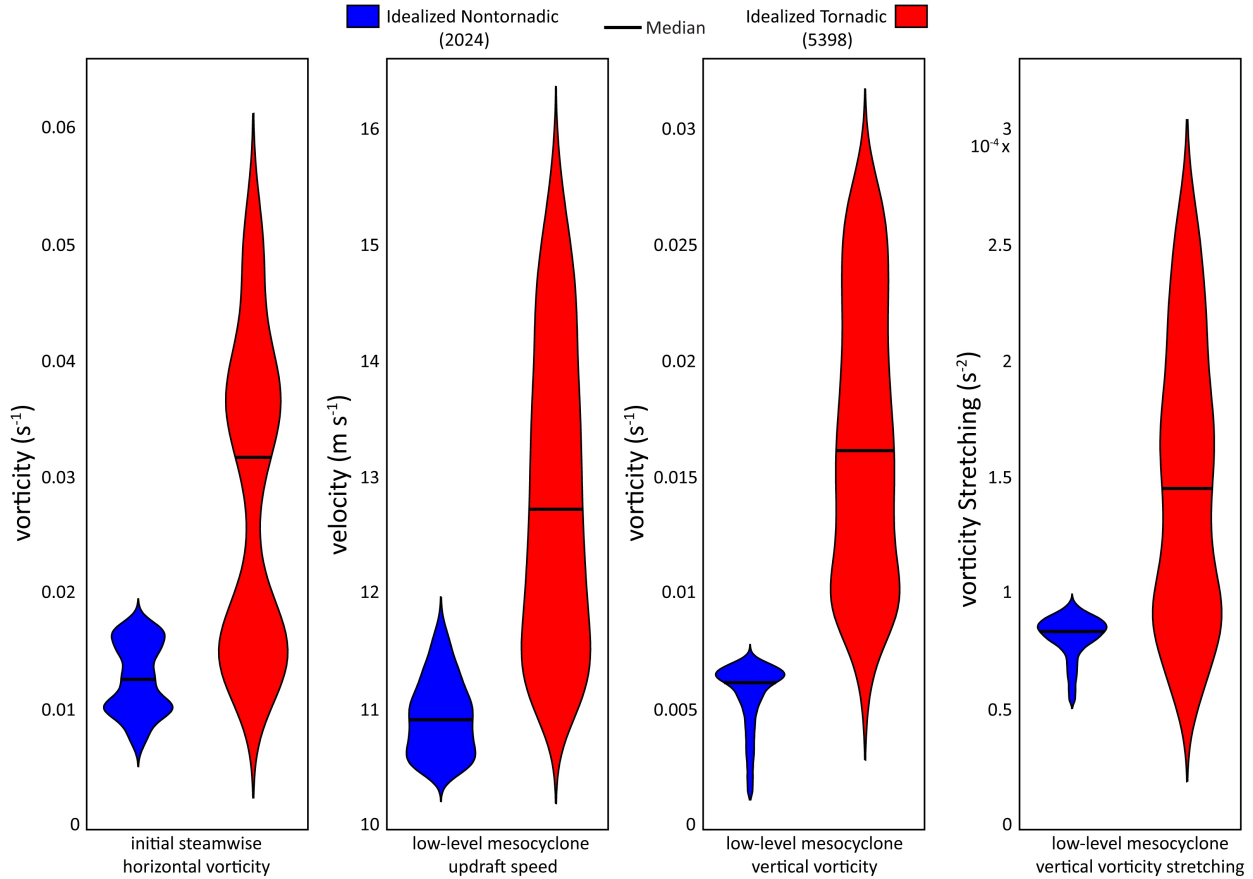
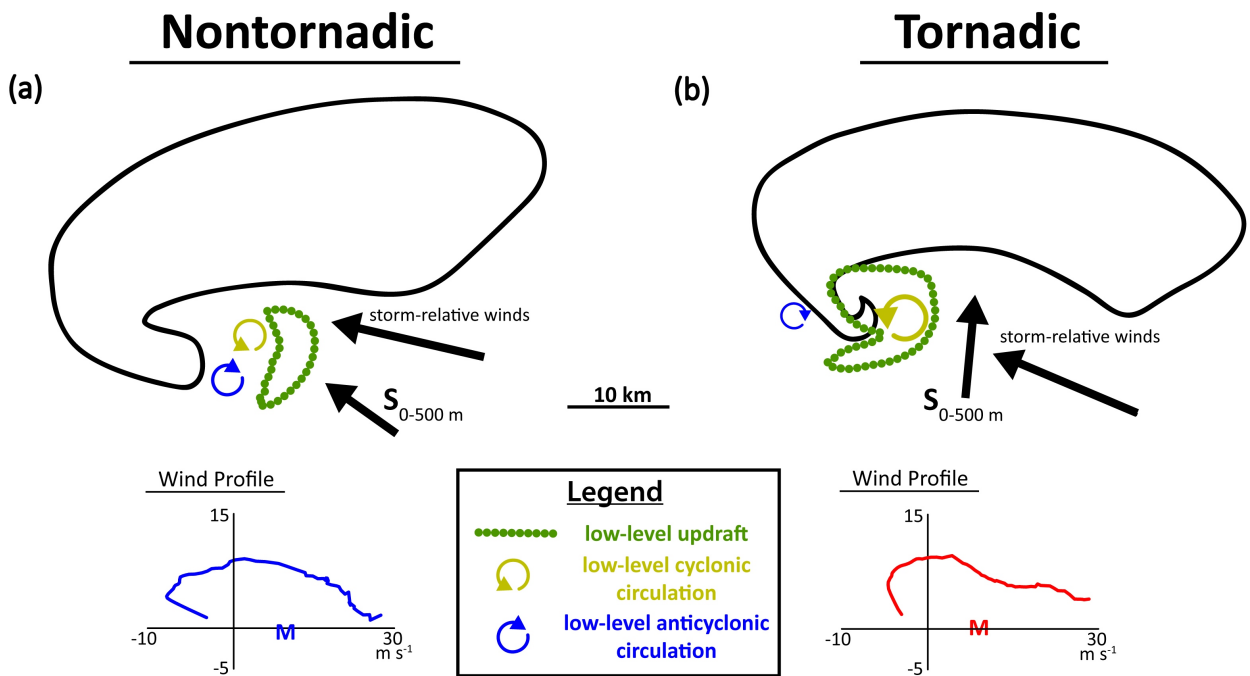


FIG. 23. Smoothed kernel density estimation violin plot of low-level mesocyclone parcel characteristics from the idealized simulations for all parcels that acquired vertical velocity of at least 10 m s^{-1} and vertical vorticity greater than 0.01 s^{-1} between 950 to 1050 m. From left to right: initial streamwise horizontal vorticity (s^{-1}), vertical velocity (m s^{-1}), vertical vorticity (s^{-1}), and vertical vorticity stretching ($\text{m}^2 \text{ s}^{-2}$) for the nontornadic (blue) and tornadic (red) idealized simulations. The black line represents the median of the distribution, and the total number of low-level mesocyclone parcels beneath the legend.



988 FIG. 24. Conceptual schematic summarizing the key differences between the (a) nontornadic and (b) tornadic
989 supercells. Schematic representations of the 0 - 500 m shear vector ($S_{0-500\text{ m}}$), low-level storm-relative winds,
990 low-level updraft (dotted green contour), cyclonic circulation maximum (yellow arrow), and anticyclonic circu-
991 lation maximum (blue arrow) presented accordingly. The shear vectors and low-level storm-relative are scaled
992 proportionally in m s^{-1} . Hodograph diagrams showing the nontornadic (blue) and tornadic (red) VORTEX2
993 wind profiles from Figure 1 are also given.